Correlated Insulators, Semimetals, and Superconductivity in Twisted Trilayer Graphene

Maine Christos,[1] Subir Sachdev,[1] and Mathias S. Scheurer[2]
[1]*Department of Physics, Harvard University, Cambridge Massachusetts 02138, USA*
[2]*Institute for Theoretical Physics, University of Innsbruck, Innsbruck A-6020, Austria*

(Received 15 June 2021; revised 23 December 2021; accepted 28 February 2022; published 25 April 2022)

Motivated by recent experiments indicating strong superconductivity and intricate correlated insulating and flavor-polarized physics in mirror-symmetric twisted-trilayer graphene, we study the effects of interactions in this system close to the magic angle, using a combination of analytical and numerical methods. We identify asymptotically exact correlated many-body ground states at all integer filling fractions ν of the flat bands. To determine their fate when moving away from these fine-tuned points, we apply self-consistent Hartree-Fock numerics and analytic perturbation theory, with good agreement between the two approaches. This allows us to construct a phase diagram for the system as a function of ν and the displacement field, the crucial experimental tuning parameter of the system, and study the spectra of the different phases. The phase diagram is dominated by a correlated semimetallic intervalley coherent state and an insulating sublattice-polarized phase around charge neutrality $\nu = 0$, with additional spin polarization being present at quarter ($\nu = -2$) or three-quarter ($\nu = +2$) fillings of the quasiflat bands. We further study the superconducting instabilities emerging from these correlated states, both in the absence and in the additional presence of electron-phonon coupling, also taking into account possible Wess-Zumino-Witten terms. In the experimentally relevant regime, we find triplet pairing to dominate, possibly explaining the observed violation of the Pauli limit. Our results have several consequences for experiments as well as future theoretical work and illustrate the rich physics resulting from the interplay of almost-flat bands and dispersive Dirac cones in twisted-trilayer graphene.

DOI: 10.1103/PhysRevX.12.021018

Subject Areas: Condensed Matter Physics
Strongly Correlated Materials
Superconductivity

I. INTRODUCTION

Graphene-based moiré superlattice systems have attracted considerable interest in the last few years, motivated by the strongly correlated physics they display [1–6]. While originally driven by the experimental realization of near-magic-angle twisted-bilayer graphene (TBG) [7,8], related strongly correlated moiré superlattices have emerged, such as twisted-double-bilayer graphene [9–12] and ABC-trilayer graphene on hexagonal boron nitride [13–15]. All of these systems exhibit low-energy bands which are energetically separated from the rest of the spectrum and can be tuned to be flat [16–18], enhancing the impact of correlations. The resulting correlated phenomena include interaction-induced insulating states [7,9–11,13], superconductivity [8–10,14], and nematic order [5,19–22], which are also integral parts of the phase diagrams of paradigmatic strongly correlated materials such as the cuprates. Furthermore, TBG has demonstrated that graphene moiré systems can also exhibit additional cascades of transitions that "reset" the band structure in an entire range of electron filling fractions [23,24]. This is likely related to the polarization of certain combinations of the internal "flavor" quantum numbers of the electrons in the quasiflat bands [25,26], with interesting consequences for superconductivity [25,27].

In addition to the twist angle between the layers as a tuning knob in TBG, the spectrum of twisted double-bilayer graphene can be efficiently tuned by applying a perpendicular electric displacement field D_0. Notwithstanding the interesting consequences for the correlated physics in the system [9–12,21,28,29], including the possibility of electrical control of the nematic director [22], its superconducting properties [9,10] have been found to be more fragile than in TBG. Fortunately, mirror-symmetric twisted-trilayer graphene (MSTG), which consists of three layers of graphene with alternating relative twist angles [see Fig. 2(a)], has very recently been realized experimentally [30–32] and combines the best of both worlds: It can be tuned significantly by applying a

---

perpendicular displacement field D_0 while exhibiting strong and reproducible superconductivity. These experiments indicate that MSTG also exhibits both interaction-induced resistive states around integer filling fractions ν as well as the aforementioned spontaneous band resetting in an extended region of ν with $2 \lesssim |\nu| \lesssim 3$, akin to the cascades in TBG [23,24]. As a function of D_0 and ν, the largest superconducting region is found to emerge out of this reconstructed normal state. Remarkably, Ref. [32] finds that the superconductor can sustain an in-plane magnetic field much larger than simple estimates of the Pauli limit. One additional crucial difference between MSTG and all of the other graphene moiré systems mentioned above is that MSTG exhibits not only quasiflat bands but, at the same time, dispersive Dirac cones [30,31,33–38]. The interplay between these different types of bands and interactions likely gives rise to rich physics but also provides theoretical challenges.

So far, only very few theoretical studies of interactions in MSTG exist [39–44], and a systematic understanding of the nature and origin of possible particle-hole and superconducting instabilities as a function of ν and D_0 is still missing. The goal of this work is to help fill this gap by providing a detailed theoretical study of electron-electron interactions in the normal state of MSTG, allowing for a large class of possible instabilities, which is then used to analyze the order parameter and origin of the different superconducting phases of the system. In order to tackle the challenges associated with the simultaneous presence of flat and dispersive bands, we use a combination of analytical and numerical approaches.

A. Summary of theoretical approach and results

Because of the length of the paper, here we provide a concise description of the theoretical approach taken and the results obtained; the latter are further described and discussed in the context of recent experiments [30–32] on MSTG in Sec. I B below.

We start from the limit without displacement field $D_0 = 0$, where the *noninteracting* band structure of the system is just that of TBG and single-layer graphene [33–38]; these two “subsystems” are, however, coupled by the Coulomb interaction. In the limit where the TBG bands are perfectly flat, we construct exact eigenstates of the interacting Hamiltonian of MSTG at all integer ν, which are also shown to be ground states for a finite range of the strength of the interaction between the two subsystems. This analysis shows that, in certain limits, also the *interacting* ground states of MSTG are given by those of TBG and single-layer graphene. This is consistent with experiment [30,31] observing a graphene Dirac cone at small D_0.

To be able to address $D_0 \neq 0$ and more realistic system parameters, we use Hartree-Fock (HF) numerics and analytic perturbation theory. Our HF approach is motivated by the success of this approach in TBG [45–50] and the fact that the exact ground states at $D_0 = 0$ are Slater-determinant states (in the TBG sector). In the analytic perturbation theory, we start from the exact ground states and study the D_0-induced deformations of the interaction matrix elements and band structure, the possible ordering in the graphene bands, the mixing between the graphene and TBG sectors for $D_0 \neq 0$, as well as the finite bandwidth of the TBG bands as perturbations. This analysis complements our HF numerics, as it allows us to pinpoint the novel energetic contributions in MSTG as compared to TBG and serves as an important validation of our numerics—in particular, concerning the fate of the graphene Dirac cones, which provides a challenge to any numerical study as they are energetically degenerate with the TBG bands only in a small fraction of the moiré Brillouin zone (MBZ). In our analytics, we take advantage of this fraction being small and use it as an expansion parameter. Overall, we find good agreement between the HF numerics and the perturbation theory, both confirming the form of the exact eigenstates at $D_0 = 0$ (but with realistic system parameters); discrepancies between the approaches are traced back to the impact on the energetics coming from additional remote bands taken into account only in the numerics.

Having established the correlated nature and possible particle-hole instabilities in the normal state of MSTG as a function of D_0 and ν, we analyze the consequences for superconductivity. We study superconductivity both in the additional presence and absence of flavor polarization. Motivated by experiments [51–53] on TBG, which indicate that electron-phonon coupling is important for pairing, we follow Ref. [54] and assume that electron-phonon coupling stabilizes superconductivity but leaves singlet and triplet almost degenerate. Informed by the results for particle-hole instabilities in MSTG, we can then investigate which of the two will be favored due to additional particle-hole fluctuations. We also discuss purely electronic pairing and comment on the relevance of Dirac cones and associated Wess-Zumino-Witten (WZW) terms, as studied previously in TBG [25,55].

B. Connection with experiment and phase diagram

To further describe and illustrate our main findings, here we discuss their consequences for the phase diagram of MSTG (see Fig. 1) and their relation to experiment [30–32]. Based on our exact ground states, perturbation theory, and HF numerics, the (for $\nu \neq 0$ slightly doped) semimetallic nature of the graphene sector is expected to be stable against interactions for $D_0 = 0$. At charge neutrality $\nu = 0$, the leading instability is found to be an intervalley coherent state (IVC) in the TBG sector. While the two sectors start to mix when $D_0 \neq 0$, the semimetallic character of the bands is retained; the Landau fan sequence of this state $\pm 2, \pm 6, \pm 10, \ldots$ is consistent with that observed in Ref. [31]. Once D_0 increases beyond a certain critical value D_0^c [which depends on the relaxation parameter

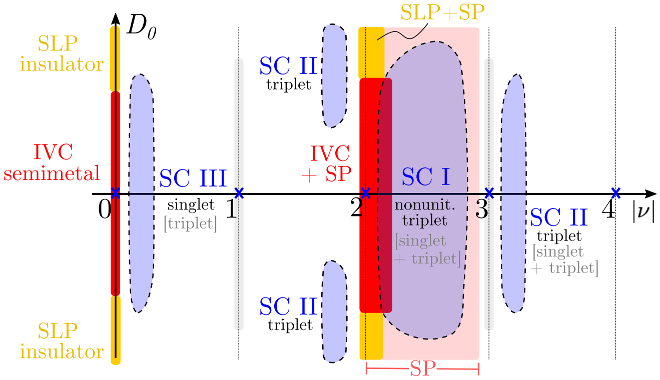

FIG. 1. Schematic phase diagram for MSTG based on our analysis, as a function of displacement field D_0 and filling fraction ν. Because of particle-hole symmetry of our model, the phase diagram depends only on $|\nu|$. We show the form of the dominant particle-hole instabilities, the intervalley-coherent (IVC) semimetallic phase, and a sublattice-polarized (SLP) insulator at $\nu = 0$ (charge neutrality); the IVC and SLP state coexist with spin polarization (SP) around $|\nu| = 2$. We discuss three different types of superconducting regimes labeled SC I–III. We indicate in black their respective spin structure for the expected sign of the intervalley Hund's coupling J_H resulting from Coulomb interactions alone (with opposite sign in gray).

w_0/w_1 in Eq. (2.3)], the IVC state transitions into a sublattice-polarized (SLP) phase, where all Dirac cones are gapped out, leading to an insulator. For realistic parameters, we expect D_0^c to be of the order of or potentially slightly larger than the range of the experimentally applied fields [30–32].

At $|\nu| = 2$, we find self-consistent HF solutions with spin polarization, which coexists with additional particle-hole instabilities. At small D_0, the leading additional symmetry-breaking state is again an IVC phase. Here, the TBG bands are completely spin polarized, while the graphene cones' polarization is only partial and approaches zero as $D_0 \rightarrow 0$. The spin polarization is our proposed mechanism for the experimentally observed band reset and reduced flavor number [30,31]. At larger D_0, the IVC transitions into a SLP state. In Sec. VI B, we discuss how the band structures we find can give rise to the experimentally observed [30] additional sign change of the Hall density at sufficiently large D_0. Our obtained behavior at $|\nu| = 0$, 2 also agrees with another experimental feature: The conductance is suppressed [30,31] at $\nu = 0$ for both $D_0 = 0$ and $D_0 > 0$, while the suppression at $|\nu| = 2$ sets in only above a finite critical value of D_0, which is consistent with the IVC (SLP) being semimetallic (insulating) at $\nu = 0$ and metallic (semimetallitc) at $|\nu| = 2$.

As we discuss in detail in Sec. V F, the relative spin orientation of these orders in the two valleys depends on the sign of the intervalley Hund's coupling J_H [see Eq. (3.16)], which is not part of the Hamiltonian for our Hartree-Fock computations; the value or sign of J_H is not determined in our computations. For $J_H < 0$, which is expected for Coulomb interactions, both the SLP and SP have the same spin polarization in the two valleys, while the IVC order parameter does not carry any spin.

As indicated in blue in Fig. 1, we investigate three different regimes of superconducting phases. For superconductivity (SC I) in the presence of spin polarization with or without additional IVC order, the order parameter will be a nonunitary triplet for $J_H < 0$ and an admixed singlet-triplet phase [27] for $J_H > 0$. For superconducting phases (SC II) close to or in the range $2 \lesssim |\nu| \lesssim 3$ but not coexisting with additional particle-hole instabilities, we expect triplet (a singlet-triplet admixed phase) to dominate for $J_H < 0$ ($J_H > 0$). All of these superconducting states are consistent [27] with the observed [32] behavior in low to intermediate magnetic fields. Finally, our analysis indicates that a superconducting phase (if present) close charge neutrality (SC III) should be in a singlet state for $J_H < 0$.

C. Organization of the paper

The remainder of the paper is organized as follows. In Sec. II, we introduce the model for the MSTG we study, its symmetries, and establish the basic notation used in this work. We begin our discussion of correlated physics in the limit of vanishing displacement field in Sec. III, where we construct exact ground states. These build the starting point for our HF numerics (see Sec. IV for $\nu = 0$ and Sec. VI for $|\nu| = 2$) and our analytical perturbation theory presented in Sec. V. Furthermore, superconducting instabilities are analyzed in Sec. VII. Finally, Sec. VIII contains a short summary and discussion of the results.

For a streamlined reading of the manuscript, we recommend starting with Secs. I A and I B and then continuing with Sec. VIII. The latter contains references to the different parts of the manuscript, where more details on the respective findings can be found.

II. MODEL AND SYMMETRIES

In this section, we introduce the interacting model we consider in this work, which consists of a continuum model to describe the moiré bands supplemented by Coulomb repulsion. We further discuss its symmetries and define the notation used in the remainder of the paper.

A. Continuum model and symmetries

MSTG is constructed from three parallel sheets of graphene where the top ($l = 1$) and bottom ($l = 3$) graphene layers are aligned with one another, and the middle ($l = 2$) layer of graphene is twisted at a relative angle θ with respect to the top and bottom layers, as shown in Fig. 2(a). To compute the noninteracting band structure, we employ a continuum-model description, which is just a three-layer extension of the frequently applied continuum model for TBG [16–18]. Denoting the electronic creation

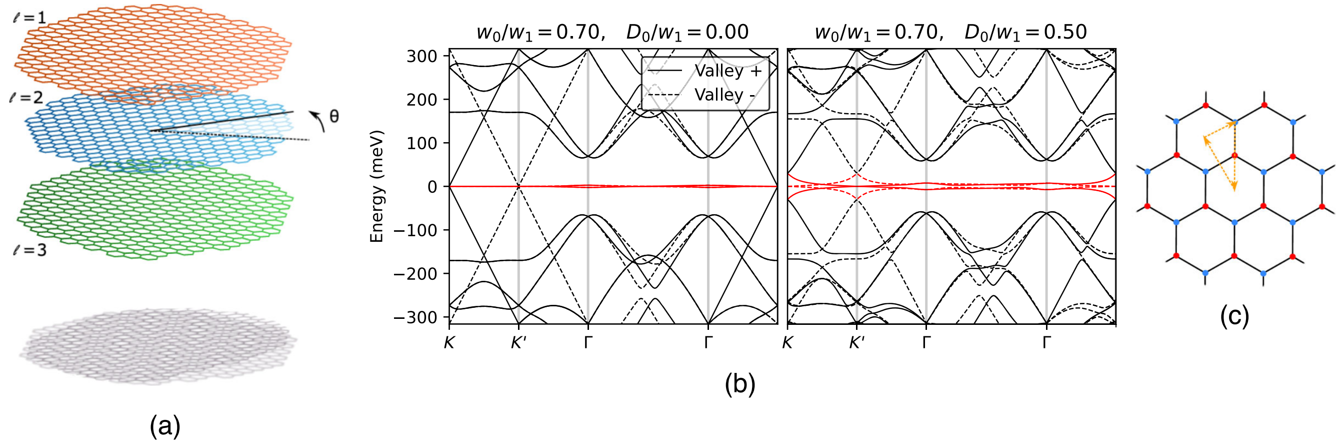

FIG. 2. (a) Schematic of the geometry of MSTG. The top and bottom layers shown in red and green, respectively, are aligned, while the middle layer (blue) is twisted at relative angle θ to the top and bottom layers. (b) Band structure of MSTG at $D_0 = 0$ (left) and $D_0 > 0$ (right) for $w_1 = 124$ meV and twist angle $\theta = 1.53°$ along the one-dimensional cut through the MBZ shown in (c). We represent the spin-degenerate bands in the two different valleys $\eta = \pm$ with solid ($\eta = +$) and dotted ($\eta = -$) lines. At $D_0 = 0$, the band structure is given by that of TBG and single-layer graphene, and we color the (two per spin and valley) quasiflat TBG bands red. For $D_0 > 0$, the bands of these two subsystems mix, but we continue to label the two bands per spin and valley closest to the Fermi as "TBG-like" bands indicated in red.

operator for an electron at position $\boldsymbol{r} \in \mathbb{R}^2$, in sublattice $\rho = 1, 2$, layer $l = 1, 2, 3$, valley $\eta = \pm$, and of spin $s = \uparrow, \downarrow$ by $c^\dagger_{\boldsymbol{r};\rho,l,\eta,s}$, the Hamiltonian reads in the absence of a displacement field as [33–36]

$$H^{\text{full}}_{0,1} = \int_{\boldsymbol{r}} c^\dagger_{\boldsymbol{r};\rho,l,\eta,s}(-i v_F (\boldsymbol{\rho}^\eta_{\theta_l})_{\rho,\rho'} \cdot \boldsymbol{\nabla}) c_{\boldsymbol{r};\rho',l,\eta,s} + \int_{\boldsymbol{r}} [c^\dagger_{\boldsymbol{r};\rho,l,\eta,s}(T_{\eta,\boldsymbol{r}})_{\rho,\rho'} c_{\boldsymbol{r};\rho',l+1,\eta,s} + \text{H.c.}], \tag{2.1}$$

where summation over repeated indices is implied, $\theta_l = (-1)^l \theta/2$, $(\boldsymbol{\rho}^{\eta=+}_\theta)_j = e^{i\theta\rho_z/2}\rho_j e^{-i\theta\rho_z/2}$, with ρ_j representing Pauli matrices in sublattice space (throughout, we use the same symbol for Pauli matrices and their indices, i.e., s_j, η_j are Pauli matrices in spin and valley space), and $\boldsymbol{\rho}^{\eta=-}_\theta = -(\boldsymbol{\rho}^{\eta=+}_\theta)^*$. While the first term in Eq. (2.1) describes the Dirac cones of the two valleys $\eta = \pm$ of each individual graphene layer in the continuum expansion around their respective K_g and K'_g points, the second line captures the tunneling between adjacent graphene layers parametrized by $T_{\eta,\boldsymbol{r}}$ (the direct hopping process between the outer two layers is neglected). As a consequence of the moiré superlattice, these tunneling matrix elements are modulated spatially. As is common, we focus on the lowest moiré-lattice harmonics for which symmetry allows for only two independent parameters w_0 and w_1 in $T_{\eta,\boldsymbol{r}}$. It can be written as [17]

$$T_{+,\boldsymbol{r}} = e^{-i\boldsymbol{q}_1\boldsymbol{r}}[\mathcal{T}_1 + \mathcal{T}_2 e^{-i\boldsymbol{G}^M_1\boldsymbol{r}} + \mathcal{T}_3 e^{-i(\boldsymbol{G}^M_1+\boldsymbol{G}^M_2)\boldsymbol{r}}], \tag{2.2}$$

and $T_{-,\boldsymbol{r}} = (T_{+,\boldsymbol{r}})^*$. Here, $\boldsymbol{q}_1 = k_\theta(0,-1)$, $k_\theta = 2|K_g|\sin(\theta/2)$ connects the K and K' points of the moiré lattice, and $\boldsymbol{G}^M_1 = -\sqrt{3}k_\theta(1,\sqrt{3})^T/2$ and $\boldsymbol{G}^M_2 = \sqrt{3}k_\theta(1,0)^T$ are the basis vectors of the reciprocal lattice (RL) of the moiré lattice RL $:= \{\sum_{j=1,2} n_j \boldsymbol{G}^M_j, n_j \in \mathbb{Z}\}$. The matrices $\mathcal{T}_j$ in sublattice space in Eq. (2.2) are given by

$$\mathcal{T}_j = w_0\rho_0 + w_1\begin{pmatrix} 0 & \omega^{j-1} \\ \omega^{-(j-1)} & 0 \end{pmatrix}, \qquad \omega = e^{-2\pi i/3}. \tag{2.3}$$

While rigidly rotated graphene layers correspond to $w_0 = w_1$, lattice relaxation [56,57] leads to $w_0 \neq w_1$. Here we consider w_0 as a free parameter and study the physics as a function of it.

As a result of the moiré modulations in Eq. (2.2), the tunneling matrix elements between the layers couple momenta related by RL vectors, which reconstructs the graphene cones of the first line in Eq. (2.1), leading to a (technically infinite) set of bands; the band energies are denoted by $\epsilon_{n,\eta}(\boldsymbol{k})$, $n \in \mathbb{Z}$, where $\boldsymbol{k}$ is in the first MBZ and we already used that Eq. (2.1) is diagonal in the valley η and trivial in the spin index s; this symmetry of the tunneling matrix elements makes the band energies independent of spin and allows us to label them by their valley index.

MSTG is distinguished from other moiré systems, such as TBG or twisted-double-bilayer graphene by a reflection symmetry σ_h under exchange of the top and bottom layers of MSTG, with action $\sigma_h : c_{\boldsymbol{r};\rho,l,\eta,s} \to c_{\boldsymbol{r};\rho,\sigma_h(l),\eta,s}$ where $\sigma_h(2) = 2$, $\sigma_h(1) = 3$, and $\sigma_h(3) = 1$. We note that a recent experiment [58] has demonstrated that this reflection symmetry is restored locally by lattice relaxation, even if the top and bottom layers are not perfectly aligned. Since σ_h acts trivially in all internal indices (ρ, η, s) and $\boldsymbol{r}$, the Hamiltonian (2.1) can be decomposed into sectors with different mirror eigenvalues $\sigma_h = \pm 1$ by performing a unitary transformation $V \in \mathrm{U}(3)$ in layer space only, $c_{\boldsymbol{r};\rho,l,\eta,s} = V_{l,\ell} \psi_{\boldsymbol{r};\rho,\ell,\eta,s}$. As was pointed out before [33] and detailed in the Supplemental Material [59] Sec. A. 1, the Hamiltonian in the mirror-even sector ($\sigma_h = +1$, $\ell = 1$, 2) turns out to be that of TBG with an interlayer hopping renormalized by a factor of $\sqrt{2}$. In the mirror-odd sector ($\sigma_h = -1$, $\ell = 3$), the Hamiltonian is that of single-layer graphene (without any moiré modulation). This can be clearly seen in the spectrum shown in Fig. 2(b), which exhibits two almost-flat TBG-bands (shown in red) per spin and valley and unreconstructed Dirac cones at K (K') associated with the graphene sector of valley $\eta = +$ ($\eta = -$). As such, there are three Dirac cones at K (and three at K'), one belonging to the graphene sector of MSTG in a single valley only and two Dirac crossings belonging to the TBG sector of both valleys. As can be seen, there are additional remote bands of both subspaces due to backfolding into the MBZ.

In addition to reflection symmetry, the Hamiltonian in Eq. (2.1) has more point symmetries forming the group C_{6h}: The model is invariant under threefold rotational symmetry C_{3z} with action $C_{3z}\colon c_{\boldsymbol{r}} \to e^{i[(2\pi)/3]\rho_z \eta_z} c_{C_{3z}\boldsymbol{r}}$, which is also an exact symmetry of the moiré lattice in Fig. 2(a). While not an exact lattice symmetry, twofold rotation perpendicular to the plane C_{2z} is a good approximate symmetry for small twist angles; in fact, it is an exact symmetry of the continuum in Eq. (2.1) which can be verified by applying its action $C_{2z}\colon c_{\boldsymbol{r}} \to \eta_x \rho_x c_{-\boldsymbol{r}}$.

In addition to these point symmetries, the model also exhibits the following exact internal symmetries: Since there is no coupling between the valleys, it is invariant under a valley U(1) transformation, $\mathrm{U}(1)_v\colon c_{\boldsymbol{r}} \to e^{i\eta_z \varphi} c_{\boldsymbol{r}}$. In combination with the absence of spin-orbit coupling, it is further invariant under the separate spin rotation in each valley, forming the group $\mathrm{SU}(2)_+ \times \mathrm{SU}(2)_-$ with $\mathrm{SU}(2)_\pm$ acting as $c_{\boldsymbol{r}} \to e^{i\boldsymbol{\varphi}\cdot \boldsymbol{s}(\eta_0 \pm \eta_z)/2} c_{\boldsymbol{r}}$. Furthermore, there is time-reversal symmetry, which is associated with the antiunitary operator Θ with $\Theta c_{\boldsymbol{r}} \Theta^\dagger = \eta_x c_{\boldsymbol{r}}$; unless stated otherwise, we always refer to this form of (spinless) time-reversal symmetry throughout the text, although combinations with spin rotations (spinful time reversal) Θ_s and with $\mathrm{U}(1)_v$ rotations $\tilde{\Theta}$ play a role further below. Since the mirror symmetry protects any mixing between the graphene and TBG subspaces and $\mathrm{U}(1)_v$ any mixing between the two valleys, the aforementioned Dirac crossings at K and K' are protected by the combination $C_{2z}\Theta$, exactly as in graphene and TBG.

Focusing on specific limits, there are also additional internal symmetries similar to TBG [46,60,61]: When $w_0 = 0$, $H_{0,1}^{\mathrm{full}}$ in Eq. (2.1) changes its sign $H_{0,1}^{\mathrm{full}} \to -H_{0,1}^{\mathrm{full}}$ if we apply the chiral symmetry operator $C\colon c_{\boldsymbol{r}} \to \rho_z L_C c_{\boldsymbol{r}}$ where L_C is a matrix in layer space given by $L_C = V \mathrm{diag}(1, 1, -1) V^\dagger$. Therefore, $w_0 = 0$ is referred to as the chiral limit [60]. Among other consequences for the interaction terms to be discussed below, the band structure has to be symmetric about zero energy at every given momentum $\boldsymbol{k}$ when $w_0 = 0$, i.e., $\mathrm{spec}_{\boldsymbol{k},\eta} = -\mathrm{spec}_{\boldsymbol{k},\eta}$, with $\mathrm{spec}_{\boldsymbol{k},\eta} = \{\epsilon_{n,\eta}(\boldsymbol{k}), n \in \mathbb{Z}\}$.

Finally, when the additional rotation of the sublattice matrices in the first line of Eq. (2.1) is neglected, $\boldsymbol{\rho}_{\theta_l}^{\eta} \to \boldsymbol{\rho}_{\theta=0}^{\eta}$, the "unitary particle-hole symmetry" previously discussed in TBG [46,61] can be extended to MSTG: Defining the unitary operator P which acts as $P\psi_{\boldsymbol{r};l=1}P^\dagger = \eta_z \psi_{-\boldsymbol{r};l=2}$, $P\psi_{\boldsymbol{r};l=2}P^\dagger = -\eta_z \psi_{-\boldsymbol{r};l=1}$, and $P\psi_{\boldsymbol{r};l=3}P^\dagger = i\rho_y \eta_y \psi_{-\boldsymbol{r};l=3}$, one finds $PH_{0,1}^{\mathrm{full}}P^\dagger = -H_{0,1}^{\mathrm{full}}$, showing that the spectrum must obey $\mathrm{spec}_{\boldsymbol{k}} = -\mathrm{spec}_{-\boldsymbol{k}}$ where $\mathrm{spec}_{\boldsymbol{k}} = \cup_\eta \mathrm{spec}_{\boldsymbol{k},\eta}$. Since we focus on small twist angles θ below, we always assume that $\boldsymbol{\rho}_{\theta_l}^{\eta}$ has been replaced by $\boldsymbol{\rho}_{\theta=0}^{\eta}$ in Eq. (2.1) when analyzing symmetries. We also later set $\theta = 0$ in our numerics.

For the detailed form of the model and the action of the symmetries in momentum space, we refer the reader to the Supplemental Material [59] Secs. A 1 and A 2, respectively. A brief list of the symmetries of H_0 and when they apply can be found in Table I.

The primary interaction term we consider in Eq. (2.8) will preserve the symmetries of the continuum model. However, we also consider the consequences of Hund's coupling in Eq. (3.16), which will break the $\mathrm{SU}(2)_+ \times \mathrm{SU}(2)_-$ symmetry down to a more realistic $\mathrm{SU}(2)_s$ (the group of simultaneous spin rotations in the two valleys).

B. Adding a displacement field

Motivated by recent experimental discoveries of electric-field-tunable correlated physics in MSTG [30–32], we now extend the model for MSTG in Eq. (2.1) and include a perpendicular displacement field D_0. Finite D_0 results in a potential difference between the top and bottom layers of graphene. Suppressing all indices except layer l, a displacement field is represented in the continuum model as

$$H_{0,2}^{\mathrm{full}} = D_0 \sum_{\boldsymbol{r}} [c_{\boldsymbol{r};l=1}^\dagger c_{\boldsymbol{r};l=1} - c_{\boldsymbol{r};l=3}^\dagger c_{\boldsymbol{r};l=3}], \tag{2.4}$$

and the full Hamiltonian becomes $H_0^{\mathrm{full}} = H_{0,1}^{\mathrm{full}} + H_{0,2}^{\mathrm{full}}$. The displacement field D_0 breaks the mirror symmetry σ_h, resulting in hybridization between bands in the TBG and graphene sectors; this hybridization can take place only between graphene and TBG bands of the same valley and spin flavor, as $\mathrm{U}_v(1)$ and spin-rotation symmetry [in fact, the full $\mathrm{SU}(2)_+ \times \mathrm{SU}(2)_-$] are preserved by $H_{0,2}^{\mathrm{full}}$.

Furthermore, when D_0 is finite, the system retains C_{2z}, C_{3z}, leading to the point group C_6. Time-reversal symmetry Θ, and in the limit $w_0 = 0$, chiral symmetry C, also persist. However, the unitary particle-hole symmetry P is no longer an exact symmetry for finite D_0.

At the K (K') point of the MBZ, the Dirac crossings which belong to the valley $\eta = +$ ($\eta = -$) will hybridize as D_0 increases with the graphene bands of the same valley which also exhibit a Dirac cone at the Fermi level; this results in the Dirac points, which are pinned at the Fermi level at $D_0 = 0$, being pushed away from the Fermi level. As $C_{2z}\Theta$ symmetry is preserved for $D_0 \neq 0$, these Dirac crossings cannot be gapped out. As a consequence of the absence of a graphene cone to hybridize with, the Dirac point of TBG in the other valley $\eta = -$ $(\eta = +)$ remains pinned at the Fermi level as D_0 increases. These features can be clearly observed in the band structure of MSTG with finite displacement field shown in Fig. 2(b).

C. Projected low-energy model

In order to make the analytical and numerical study of interactions feasible in the system, we restrict our Hamiltonian to a finite set of bands in the vicinity of the Fermi level. Going forward, we denote the two bands closest to the Fermi level per spin and valley as TBG-like bands and the next two closest bands per spin and valley as graphenelike bands. All other bands at energies further away from the Fermi level are referred to as remote bands. When $D_0 = 0$, the TBG-like bands are labeled by mirror-symmetry eigenvalue $\sigma_h = +1$ and can be identified exactly with the two flat bands of TBG. The graphenelike bands at $D_0 = 0$ are identified exactly with the bands of the continuum model of graphene in the vicinity of the K and K' points. For finite D_0, the bands with different eigenvalues hybridize, but we retain our naming convention for the four bands closest to the Fermi level; i.e., the bands indicated in red in Fig. 2 are TBG-like bands.

Note that away from the K points, the graphenelike bands are technically identified with the first remote bands of TBG with $\sigma_h = +1$ for $D_0 = 0$ within this convention. In our analytical calculations below, however, we restrict the analysis to the TBG-like bands in the full MBZ and to the graphenelike bands only in the vicinity of the K and K' points where they retain their graphenelike identity. Denoting the associated creation operators in these two sets of bands by $b^\dagger_{\boldsymbol{k};p,\eta,s}$ and $g^\dagger_{\boldsymbol{k};p,\eta,s}$, where $\boldsymbol{k} \in \mathrm{MBZ}$ is the momentum, $p = +$ $(p = -)$ labels the upper (lower) band in each sector, η is the valley, and s the spin quantum number of the electrons, the noninteracting Hamiltonian projected to these bands becomes

$$\begin{aligned} H_0 = &\sum_{\boldsymbol{k}\in\mathrm{MBZ}} W_{\mathrm{TBG}}\epsilon_{(b,p),\eta}(\boldsymbol{k}) b^\dagger_{\boldsymbol{k};p,\eta,s} b_{\boldsymbol{k};p,\eta,s} \\ &+ \sum_{\boldsymbol{k}\in\mathrm{MBZ}'} \epsilon_{(g,p),\eta}(\boldsymbol{k}) g^\dagger_{\boldsymbol{k};p,\eta,s} g_{\boldsymbol{k};p,\eta,s}. \end{aligned} \tag{2.5}$$

Here, the extra prime in MBZ′ in the second line indicates that we restrict the graphenelike degrees of freedom to the vicinity of the K and K' points in our analytical calculations. Note that we further introduce the dimensionless parameter $W_{\mathrm{TBG}} \in [0, 1]$ that allows us to organize the perturbation theory of Sec. V D in the TBG-like bandwidth. While the physical system corresponds to $W_{\mathrm{TBG}} = 1$, we define the flat limit as $W_{\mathrm{TBG}} = 0$, which plays an important role below. Note that the Hamiltonian in Eq. (2.1) realizes the flat limit exactly $\epsilon_{(b,p),\eta}(\boldsymbol{k}) = 0$, only when $w_0 = 0$, θ is at the magic angle, and when $D_0 = 0$.

TABLE I. Summary of discrete single-particle symmetries (denoted S) of our model and when they apply (last column). For convenience of the reader and future reference, we show a redundant set of symmetries. We also indicate whether they are unitary or antiunitary symmetries (second column) and whether they commute $+$ or anticommute $-$ (third column) with the noninteracting Hamiltonian H_0^{full}. Finally, we specify their action on the low-energy field operators in order to fix the phase of the Bloch states, using σ_j to denote Pauli matrices acting on the upper or lower bands subspace.

S	Unitary	$[\cdot,\cdot]_\pm$	$S b_{\boldsymbol{k}} S^\dagger$	$S g_{\boldsymbol{k}} S^\dagger$	Condition
C_{2z}	✓	$+$	$\eta_1\sigma_0 b_{-\boldsymbol{k}}$	$\eta_1\sigma_0 g_{-\boldsymbol{k}}$	None
C_{3z}	✓	$+$	$\eta_0\sigma_0 b_{C_{3z}\boldsymbol{k}}$	$\eta_0\sigma_0 g_{C_{3z}\boldsymbol{k}}$	None
σ_h	✓	$+$	$\eta_0\sigma_0 b_{\boldsymbol{k}}$	$-\eta_0\sigma_0 g_{\boldsymbol{k}}$	$D_0 = 0$
Θ	✗	$+$	$\eta_1\sigma_0 b_{-\boldsymbol{k}}$	$\eta_1\sigma_0 g_{-\boldsymbol{k}}$	None
Θ_s	✗	$+$	$s_2\eta_1\sigma_0 b_{-\boldsymbol{k}}$	$s_2\eta_1\sigma_0 g_{-\boldsymbol{k}}$	None
$\tilde{\Theta}$	✗	$+$	$\eta_2\sigma_0 b_{-\boldsymbol{k}}$	$\eta_2\sigma_0 g_{-\boldsymbol{k}}$	None
C	✓	$-$	$\eta_3\sigma_2 b_{\boldsymbol{k}}$	$\eta_3\sigma_2 g_{\boldsymbol{k}}$	$w_0 = 0$
P	✓	$-$	$-i\eta_3\sigma_2 b_{-\boldsymbol{k}}$	$i\eta_1\sigma_2 g_{-\boldsymbol{k}}$	$D_0 = 0$, $\boldsymbol{\rho}_{\theta\to 0}$
$C_{2z}\Theta$	✗	$+$	$\eta_0\sigma_0 b_{\boldsymbol{k}}$	$\eta_0\sigma_0 g_{\boldsymbol{k}}$	None
$C_{2z}P$	✓	$-$	$\eta_2\sigma_2 b_{\boldsymbol{k}}$	$i\sigma_2 g_{\boldsymbol{k}}$	$D_0 = 0$, $\boldsymbol{\rho}_{\theta\to 0}$

In our numerics, we keep all momenta of both sets of (in total 16) bands in Eq. (2.5) and continue to use $g^\dagger_{\boldsymbol{k};p,\eta,s}$ as creation operators for the second lowest set of bands throughout the MBZ. To check convergence, we also study the impact of adding additional remote bands, as described in the Supplemental Material [59] Sec. C 3.

In order to fix the phases of the wave functions of the TBG-like and graphenelike bands, we specify how they transform under the action of the various discrete symmetries discussed above or, equivalently how they act on the electronic operators $b^\dagger_{\boldsymbol{k};p,\eta,s}$ and $g^\dagger_{\boldsymbol{k};p,\eta,s}$. While a thorough discussion can be found in the Supplemental Material [59] Sec. A 2, these representations are summarized in Table I.

Based on these symmetry representations, one finds that the dispersions are constrained to have the form

$$\begin{aligned} \epsilon_{(b,p),\eta}(\boldsymbol{k}) = &\, p\bar{E}^b_0(\boldsymbol{k}) + \eta\bar{E}^b_1(\boldsymbol{k})w_0 \\ &+ p\eta\bar{E}^b_2(\boldsymbol{k})D_0 + \bar{E}^b_3(\boldsymbol{k})w_0 D_0 \end{aligned} \tag{2.6}$$

and

$$\epsilon_{(g,p),\eta}(\boldsymbol{k}) = p\bar{E}^g_0(\boldsymbol{k};\eta) + \bar{E}^g_1(\boldsymbol{k};\eta)w_0 D_0. \tag{2.7}$$

To illustrate the changes of the form of the band structures when symmetries are broken by $w_0 \neq 0$ and $D_0 \neq 0$, we introduce $\bar{E}^b_j(\boldsymbol{k})$ and $\bar{E}^g_j(\boldsymbol{k};\eta)$, which are functions of w_0 and D_0 that stay finite when $w_0, D_0 \to 0$.

As can be seen, the two terms in the first row of Eq. (2.6) just correspond to the TBG band structure (with $w_0 = 0$, or without $w_0 \neq 0$, chiral symmetry). The second line shows that the hybridization with the graphene bands for $D_0 \neq 0$ distorts the TBG band structure in a way not present in TBG, which is related to the D_0-induced breaking of $C_{2z}P$ symmetry. One of these additional terms leads to superexchange processes in the TBG-like bands that are not present in TBG and are discussed in Sec. V D. In Eq. (2.7), the first term $\bar{E}_0^g(\boldsymbol{k};\eta)$ simply becomes the graphene Dirac dispersion for $D_0 \to 0$. We further see that the property $\epsilon_{(g,+),\eta}(\boldsymbol{k}) = -\epsilon_{(g,-),\eta}(\boldsymbol{k})$ is violated only if w_0 and D_0 are simultaneously nonzero. This is expected, as the graphene-like bands can "feel" only the broken chiral symmetry if they hybridize with the TBG-like bands. For the parameters in Fig. 2(b), this change in dispersion is a rather weak effect around the Dirac cones.

D. Interactions and form factors

As our goal is to study the interacting behavior of MSTG, we next add interaction terms to the Hamiltonian. We assume that these interactions in the full continuum model are of the density-density form. Our full interaction Hamiltonian thus reads as

$$H_1^{\text{full}} = \frac{1}{2N}\sum_{\boldsymbol{q}} V(\boldsymbol{q}) :\rho_{\boldsymbol{q}}^{\text{full}}\rho_{-\boldsymbol{q}}^{\text{full}}:, \tag{2.8}$$

where $:\ldots:$ denotes normal ordering, N is the number of moiré sites, and $\rho_{\boldsymbol{q}}^{\text{full}}$ is the density operator of momentum $\boldsymbol{q}$ of the continuum electron operators $c_{\boldsymbol{r}}$ in Eq. (2.1). Note $\boldsymbol{q} \in \mathbb{R}$ in the sum in Eq. (2.8), which is *not* restricted to the MBZ. For our analytical discussions below, we do not have to specify the explicit form of $V(\boldsymbol{q})$ but use only $V(\boldsymbol{q}) > 0$ and $V(\boldsymbol{q}) = V(-\boldsymbol{q})$; consequently, our analytical results are valid regardless of the details of the screening processes at high energies and of nearby gates and/or substrates that affect the detailed form $V(\boldsymbol{q})$. For our numerics, we use the single-gate-screened Coulomb potential:

$$V(\boldsymbol{q}) = \frac{1 - e^{-2|\boldsymbol{q}|d_s}}{2A_{\text{moiré}}\epsilon_0\epsilon|\boldsymbol{q}|}, \tag{2.9}$$

where we normalize by the real-space area of the moiré unit cell $A_{\text{moiré}}$. We vary the screening length d_s in our numerical calculations from $d_s = 10$ to 80 nm and find relatively little dependence of the relative energies between phases and no qualitative change in the ground states. We therefore take $d_s = 40$ nm as our default value. We also vary the dielectric constant ϵ from $\epsilon = 4$ to $\epsilon = 15$. We find the phase boundaries depend on ϵ, though no new phases emerge as ϵ is varied (the effect of varying interaction parameters is further discussed in the Supplemental Material [59] Sec. C 3, especially Fig. S 2). Unless otherwise specified, we take $\epsilon = 7$.

We note that the above interaction term has all the symmetries of the continuum model introduced in Sec. II, including the $\mathrm{SU}(2)_+ \times \mathrm{SU}(2)_-$ symmetry. In the realistic system, there is Hund's coupling $J_H \neq 0$, which breaks $\mathrm{SU}(2)_+ \times \mathrm{SU}(2)_-$ down to $\mathrm{SU}(2)_s$. We discuss the form of Hund's coupling in the Supplemental Material [59] Sec. F 5 and Eq. (3.16), and note its consequences in Sec. III C.

Neglecting normal ordering and replacing $\rho_{\boldsymbol{q}}^{\text{full}} \to \tilde{\rho}_{\boldsymbol{q}}^{\text{full}} = \rho_{\boldsymbol{q}}^{\text{full}} - \text{const} \times \delta_{\boldsymbol{q},0}$ in Eq. (2.8) leads to a new form of the interaction $\tilde{H}_1^{\text{full}}$, which, however, can be rewritten as H_1^{full} by a redefinition of the chemical potential (and energy reference point). This equivalence does not hold anymore after projecting $\rho_{\boldsymbol{q}}^{\text{full}}$ and $\tilde{\rho}_{\boldsymbol{q}}^{\text{full}}$ in H_1^{full} and $\tilde{H}_1^{\text{full}}$, respectively, to a finite set of bands of H_0. As we describe in more detail in the Supplemental Material [59] Sec. A 3, we follow Refs. [46,61] and rewrite the interaction before projection such that it exhibits particle-hole symmetry with respect to the charge-neutrality point before and after projection. Denoting the electronic creation operators for band n, of valley η, spin s, and with momentum $\boldsymbol{k} \in$ MBZ by $f_{\boldsymbol{k};n,\eta,s}^\dagger$, the projected interaction becomes

$$\tilde{H}_1 = \frac{1}{2N}\sum_{\boldsymbol{q}} V(\boldsymbol{q})\delta\rho_{\boldsymbol{q}}\delta\rho_{-\boldsymbol{q}}, \tag{2.10a}$$

with the symmetrized density operators

$$\delta\rho_{\boldsymbol{q}} = \sum_{\boldsymbol{k}\in\text{MBZ}}\left[f_{\text{MBZ}(\boldsymbol{k}+\boldsymbol{q})}^\dagger F_{\boldsymbol{k},\boldsymbol{q}} f_{\boldsymbol{k}} - \frac{1}{2}\sum_{\boldsymbol{G}\in\text{RL}}\delta_{\boldsymbol{q},\boldsymbol{G}}\text{tr}(F_{\boldsymbol{k},\boldsymbol{G}})\right]. \tag{2.10b}$$

Here, $\text{MBZ}(\boldsymbol{k}) \coloneqq \boldsymbol{k} - \boldsymbol{G}_{\boldsymbol{k}} \in$ MBZ for the unique reciprocal lattice vector $\boldsymbol{G}_{\boldsymbol{k}} \in$ RL. We suppress all indices of $f_{\boldsymbol{k}}$ and $f_{\boldsymbol{k}}^\dagger$, which should be viewed as column and row vectors in band, valley, and spin space and introduce the matrix-valued form factors $F_{\boldsymbol{k},\boldsymbol{q}}$, which contain all the microscopic details of the wave functions of the bands of H_0 [see Eq. (S25) in the Supplemental Material [59] for a formal definition]. Note that Eq. (2.10) holds for any subset of bands that we want to keep. As already discussed in Sec. II C above, we keep only the TBG-like bands and graphenelike bands (around the K and K' points) in the analytics, while we allow for more bands in the HF numerics.

We refer the interested reader to the Supplemental Material [59] Sec. A 3, where a detailed discussion of the constraints on $F_{\boldsymbol{k},\boldsymbol{q}}$ resulting from symmetries, Hermiticity, and the structure of H_0 can be found, and here we state only a few properties of the form factors that we explicitly refer back to in the main text. First, as a consequence of $\mathrm{U}(1)_v$ and spin-rotation symmetry, the form factors can have only nondiagonal matrix structure in band space,

$$(F_{\boldsymbol{k},\boldsymbol{q}})_{(n,\eta,s),(n',\eta,s)} = \delta_{s,s'}\delta_{\eta,\eta'}(F_{\boldsymbol{k},\boldsymbol{q}}^\eta)_{n,n'}. \tag{2.11}$$

In accordance with our notation in Eq. (2.5), we use the multi-index notation $n = (t, p)$ where the "type" t

distinguishes between the graphenelike $t = g$ and TBG-like $t = b$ bands, and $p = +$ ($p = -$) labels the upper (lower) band; for instance, for the electronic operators, it holds $f_{\boldsymbol{k};(b,p),\eta,s} = b_{\boldsymbol{k};p,\eta,s}$ and $f_{\boldsymbol{k};(g,p),\eta,s} = g_{\boldsymbol{k};p,\eta,s}$. As a consequence of the σ_h symmetry for $D_0 = 0$, the form factors become block diagonal in the sectors with different σ_h eigenvalue. As such, $F^{tt'}_{\boldsymbol{k},\boldsymbol{q}}$ defined via

$$(F^{tt'}_{\boldsymbol{k},\boldsymbol{q}})_{(p,\eta,s),(p',\eta',s')} = \delta_{s,s'}\delta_{\eta,\eta'}(F^{\eta}_{\boldsymbol{k},\boldsymbol{q}})_{(t,p)(t',p')} \tag{2.12}$$

obeys

$$F^{tt'}_{\boldsymbol{k},\boldsymbol{q}} \propto \delta_{t,t'} \quad \text{for } D_0 = 0. \tag{2.13}$$

Consequently, the entire interacting Hamiltonian $H_0 + \tilde{H}_1$ preserves the charge in the graphene and TBG system separately. This leads to simplifications, which are exploited in Sec. III below. For $D_0 \neq 0$, this separate conservation of charge in the graphene and TBG sectors no longer holds, as the form factors in Eq. (2.12), and hence, the density operators in the interaction will *not* be diagonal in the t index and scatter electrons between the two different types of bands.

In the limit $D_0 = 0$, one can also compute the form factors in the graphene sector analytically [see Eq. (S39) in the Supplemental Material [59] for the full expression]. Most importantly for our purposes here, one finds that

$$F^{gg}_{\boldsymbol{k},\boldsymbol{G}} = \delta_{\boldsymbol{G},0}\sigma_0\eta_0 s_0, \qquad \boldsymbol{G} \in \mathrm{RL} \quad \text{for } D_0 = 0, \tag{2.14}$$

where σ_0 are Pauli matrices in the "band space" (with indices $p = \pm$). Here, only the $\boldsymbol{G} = 0$ component is finite, which is related to the fact that the graphene bands do not feel the moiré superlattice for $D_0 = 0$.

III. EXACT GROUND STATES AT $D_0 = 0$

We begin our discussion of the interacting physics in the decoupled limit defined as $D_0 = 0$, where all bands can be labeled by their mirror eigenvalue $\sigma_h = \pm 1$, and the low-energy bands are those of TBG and single-layer graphene. While one might intuitively expect that the presence of the additional graphene Dirac cones, which have a much lower density of states than the (almost) flat bands close to the magic angle of TBG, is not strong enough to change the symmetry of the correlated insulating phase of TBG, it is *a priori* not clear whether the density-density coupling between the two subsystems can also induce the same symmetry-breaking order (and potentially gap out) the graphene Dirac cones. It is further not clear whether *exact* interacting ground states of MSTG can be identified in certain limits similar to TBG [46,62,63]. These aspects are addressed in this section.

A. Hamiltonian and construction of eigenstates

To this end, let us focus on the flat limit $W_{\mathrm{TBG}} = 0$ and postpone the perturbative treatment of the finite TBG bandwidth to Sec. V D. From our discussion in Sec. II, we can read off that the low-energy Hamiltonian of MSTG in the flat-decoupled limit is given by

$$H_{\mathrm{FD}} = H^g + H^b + \lambda H^{gb} \tag{3.1}$$

consisting of three terms: H^g is the Hamiltonian of (both valleys of) single-layer graphene with Coulomb repulsion [see Eq. (S44) in the Supplemental Material [59]], and H^b the interacting Hamiltonian of TBG in the flat limit given by

$$H^b = \frac{1}{2N}\sum_{\boldsymbol{q}} V(\boldsymbol{q})\delta\rho^b_{\boldsymbol{q}}\delta\rho^b_{-\boldsymbol{q}}, \tag{3.2}$$

where we define the projected subsystem density operators

$$\delta\rho^t_{\boldsymbol{q}} = \sum_{\boldsymbol{k}\in\mathrm{MBZ}}\left[t^\dagger_{\mathrm{MBZ}(\boldsymbol{k}+\boldsymbol{q})}(F^{tt}_{\boldsymbol{k},\boldsymbol{q}})t_{\boldsymbol{k}} - \frac{1}{2}\sum_{\boldsymbol{G}\in\mathrm{RL}}\delta_{\boldsymbol{q},\boldsymbol{G}}\mathrm{tr}(F^{tt}_{\boldsymbol{k},\boldsymbol{G}})\right], \tag{3.3}$$

where $t = g, b$. Finally, the last term in Eq. (3.1) describes the coupling between the two subsystems via a density-density interaction,

$$\lambda H^{gb} = \frac{\lambda}{N}\sum_{\boldsymbol{q}} V(\boldsymbol{q})\delta\rho^g_{-\boldsymbol{q}}\delta\rho^b_{\boldsymbol{q}}, \tag{3.4}$$

where the additional prefactor $\lambda \in [0, 1]$ is introduced to adiabatically turn on the H^{gb} interaction (the physical system corresponds to $\lambda = 1$).

For $\lambda = 0$, the Hamiltonian is just the sum $H^g + H^b$ of the two commuting subsystem Hamiltonians, so its eigenstates are just given by (all combinations) of the individual eigenstates of graphene and TBG with the correct particle number. Let us fix a certain integer filling $\nu_b = 0, \pm 1, \pm 2, \pm 3, \pm 4$ of the TBG system. Then, the graphene system will be at a corresponding filling, which we write formally as $\nu_g = \nu_g(\nu_b)$, and its ground state will be a semimetal with ($\nu_g = 0$) or without ($\nu_g \neq 0$) doping, that exhibits correlations but does not spontaneously break any symmetries; these properties are well established (theoretically and experimentally) for graphene [64]. Let us denote the ground state of the graphene system at filling $\nu_g = \nu_g(\nu_b)$ by $|\Psi^g_0(\nu_b)\rangle$ and its (gapless) excited states with the same particle number by $|\Psi^g_j(\nu_b)\rangle$, $j > 0$. In the hypothetical absence of any correlations in the graphene subspace, $|\Psi^g_0(\nu_b)\rangle$ [$|\Psi^g_j(\nu_b)\rangle$] would just be Slater-determinant state(s) with the Dirac cones filled up to the chemical potential (and some additional particle-hole excitations).

Exact ground states of the flat-band TBG Hamiltonian in Eq. (3.2) have been discussed previously [46,62,63], which we very briefly review here using our notation in order to set the stage for the extension to MSTG. Upon defining new operators according to (referred to as "chiral basis" in Ref. [61]; in this basis, the chiral form factors [see Eq. (S47) in the Supplemental Material [59]] are diagonal)

$$\tilde{b}_{\boldsymbol{k};c,\eta,s} = U_{c,p} b_{\boldsymbol{k};p,\eta,s}, \qquad U = \frac{1}{\sqrt{2}} \begin{pmatrix} 1 & -i \\ 1 & i \end{pmatrix}, \tag{3.5}$$

consider the set of states

$$|\Psi_0^b(\nu_b)\rangle = \prod_{\boldsymbol{k}\in \mathrm{MBZ}} \prod_{c=\pm} \prod_{j_c=1}^{\nu_c} \tilde{b}^\dagger_{\boldsymbol{k};c,\eta^c_{j_c},s^c_{j_c}} |0^b\rangle \tag{3.6}$$

with arbitrary combinations of occupied flavors $\{\eta_j^\pm, s_j^\pm\}$ such that $\nu_+ + \nu_- = 4 + \nu_\mathrm{b}$. It was shown in Ref. [62] that

$$\delta\rho_{\boldsymbol{q}}^b |\Psi_0^b(\nu_b)\rangle = \sum_{\boldsymbol{G}\in \mathrm{RL}} \delta_{\boldsymbol{q},\boldsymbol{G}} R_{\boldsymbol{G}} |\Psi_0^b(\nu_b)\rangle, \tag{3.7}$$

with $R_{\boldsymbol{G}} = \nu_b \sum_{\boldsymbol{k}} \mathrm{tr}[F^{bb}(\boldsymbol{k},\boldsymbol{G})]/8$ when $w_0 = 0$, i.e., in the chiral limit. As such, all of these states are exact eigenstates of H^b in Eq. (3.2). References [46,62] further showed that these states will always be ground states of H^b for $\nu_b = 0$; the same holds for all other integers ν_b as long as the flat-metric condition

$$F^{bb}_{\boldsymbol{k},\boldsymbol{G}} = \mathbb{1} f(\boldsymbol{G}), \quad \forall\, \boldsymbol{k},\boldsymbol{G} \tag{3.8}$$

is not violated by a significantly large amount. Furthermore, when turning on $w_0 \neq 0$, the subset of states in Eq. (3.6) with $\eta_j^+ = \eta_j^-$ and $s_j^+ = s_j^-$, which are necessarily at even integer ν_b, still obey Eq. (3.7) and remain ground states of H_b [unless $\nu_b = \pm 2$ and Eq. (3.8) is sufficiently violated]. The additional states which obey Eq. (3.7), like the sublattice-polarized states, are disfavored away from the chiral limit as they acquire energy penalties proportional to w_0 (as we also explicitly see in Sec. V A and Table III below).

Having established the spectrum of H_FD in Eq. (3.1) for $\lambda = 0$, let us next discuss what happens once λ is turned on. Using the fact that the graphene form factors obey Eq. (2.14), one can rewrite H^{gb} in the low-energy spectrum of MSTG as (see the Supplemental Material [59] Sec. B 1 for details)

$$H^{gb} = \frac{1}{N} \sum_{\boldsymbol{q}} V(\boldsymbol{q}) \delta\rho^g_{-\boldsymbol{q}} \left(\delta\rho^b_{\boldsymbol{q}} - \sum_{\boldsymbol{G}\in\mathrm{RL}} \delta_{\boldsymbol{q},\boldsymbol{G}} R_{\boldsymbol{G}} \right) + E_0(\nu_b). \tag{3.9}$$

In the above, $E_0(\nu_b)$ is proportional to the filling of the graphene Dirac cones ν_g when the flat metric condition holds, and is therefore a constant at integer fillings where the TBG bands are known (and verified in our numerics) to be gapped. So we immediately see that the property (3.7) of all of the exact TBG states $|\Psi_0^b(\nu_b)\rangle$ defined above implies

$$H^{gb} |\Psi_j^g(\nu_b)\rangle |\Psi_0^b(\nu_b)\rangle = E_0(\nu_b) |\Psi_j^g(\nu_b)\rangle |\Psi_0^b(\nu_b)\rangle. \tag{3.10}$$

Consequently, all of the states $|\Psi_j^g(\nu_b)\rangle|\Psi_0^b(\nu_b)\rangle$ remain *exact* eigenstates of the full MSTG Hamiltonian H_FD in the flat-decoupled limit at arbitrary λ.

Whether the states $|\Psi_0^g(\nu_b)\rangle|\Psi_0^b(\nu_b)\rangle$ will also remain the exact ground states is a more subtle question: Since the states $|\Psi_0^b(\nu_b)\rangle$ break symmetries, $H_\mathrm{FD}|_{\lambda=0}$ will have a gapless Goldstone spectrum. In principle, an arbitrarily small λ could lower the energy of some of those states below that of $|\Psi_0^g(\nu_b)\rangle|\Psi_0^b(\nu_b)\rangle$. However, we show in Supplemental Material [59] Sec. B 2 that is not the case if $\nu_b = 0$ or $w_0 = 0$, or if Eq. (3.8) holds. Therefore, a finite $\lambda > 0$ is required before $|\Psi_0^g(\nu_b)\rangle|\Psi_0^b(\nu_b)\rangle$ cease to be the exact ground states.

B. Discussion of ground states

Taken together, we show that the states $|\Psi_j^g(\nu_b)\rangle|\Psi_0^b(\nu_b)\rangle$ where $|\Psi_j^g(\nu_b)\rangle$ is just the spectrum of single-layer graphene at filling $\nu_g = \nu_g(\nu_b)$ and $|\Psi_0^b(\nu_b)\rangle$ is any of the states in Eq. (3.6) are exact eigenstates of the MSTG Hamiltonian in the chiral-flat-decoupled limit ($w_0 = W_\mathrm{TBG} = D_0 = 0$), $H_\mathrm{FD}|_{w_0=0}$, for any integer ν_b. Furthermore, there is a finite region of λ for which $|\Psi_0^g(\nu_b)\rangle|\Psi_0^b(\nu_b)\rangle$ will remain a ground state of MSTG if $|\Psi_0^b(\nu_b)\rangle$ is a ground state of TBG [recall that $|\Psi_0^b(\nu_b)\rangle$ is guaranteed to be a ground state of TBG for $\nu_b = 0$ without further assumptions while it requires that the flat-metric condition is not too strongly violated for $\nu_b \neq 0$]. Finally, away from the chiral limit $w_0 \neq 0$, the subset of states in Eq. (3.6) with $\eta_j^+ = \eta_j^-$ and $s_j^+ = s_j^-$ are known to be ground states of TBG in the flat limit for integer ν_b and if the flat metric condition holds [62]. Our analysis shows that these states remain exact eigenstates for $\lambda \neq 0$ and also ground states for $|\lambda| < \lambda_c > 0$ in the non-chiral-flat-decoupled limit ($W_\mathrm{TBG} = D_0 = 0$, $w_0 \neq 0$).

In all of these limits, we see that the graphene subsystem retains its (correlated but symmetry-unbroken and, depending on ν_b, doped) semimetallic properties for all integer filling fractions ν_b. This is consistent with experiment, where quantum oscillations indicate a dispersive Dirac cone at $D_0 = 0$ [30,31]. Furthermore, the exact eigenstates established above are used as our starting point for further analytical considerations in Sec. V and their product-state nature motivates our HF numerical study of the problem in Sec. IV. Both numerics and analytics complement the discussion presented above by (i) validating the stability of the Dirac cones at $D_0 = 0$ in schemes that do not rely on λ being small and (ii) by tuning away from the exactly solvable limits ($W_\mathrm{TBG} = D_0 \neq 0$) and (iii), for the numerics, including additional remote bands.

C. Resultant candidate states

To build the foundation for these additional analytical and numerical computations, we use the exact (and highly degenerate) ground states established above in the chiral-flat-decoupled limit to construct a finite set of candidate phases and their respective order parameters.

We first define the correlation matrix $P_{\boldsymbol{k}}$ with elements

$$(P_{\boldsymbol{k}})_{(t,p,\eta,s),(t',p',\eta',s')} \coloneqq \langle\Psi_0| f^\dagger_{\boldsymbol{k};(t,p),\eta,s} f_{\boldsymbol{k};(t',p'),\eta',s'} |\Psi_0\rangle \quad (3.11)$$

to characterize a given ground state $|\Psi_0\rangle$ of MSTG. Hermiticity implies $P_{\boldsymbol{k}}^\dagger = P_{\boldsymbol{k}}$. As is common, we further write $P_{\boldsymbol{k}} = \frac{1}{2}(\mathbb{1} + Q_{\boldsymbol{k}})$ and use $Q_{\boldsymbol{k}}$ as our “order parameter” to characterize the (potentially symmetry-broken) structure of $|\Psi_0\rangle$. It must obey

$$Q_{\boldsymbol{k}}^\dagger = Q_{\boldsymbol{k}}, \qquad \frac{1}{N}\sum_{\boldsymbol{k}} \mathrm{tr}[Q_{\boldsymbol{k}}] = \nu_b + \nu_g \equiv \nu. \quad (3.12)$$

As we see above, the ground states of MSTG in the flat-decoupled limit ($W_{\mathrm{TBG}} = D_0 = 0$) obey

$$(Q_{\boldsymbol{k}})_{(t,p,\eta,s),(t',p',\eta',s')} = \delta_{t,t'} (Q^t_{\boldsymbol{k}})_{(p,\eta,s),(p',\eta',s')}; \quad (3.13)$$

i.e., they do not exhibit any “coherence” between the graphene and TBG sectors. This is expected, as the presence of σ_h requires any order parameter to be either even (diagonal in t space) or odd (off-diagonal) under σ_h; due to the large density of states in the TBG sector, we expect the former mirror-symmetry-even order parameters to dominate. Once $D_0 \neq 0$, mixing is allowed, as we see in our numerics below and discuss in detail analytically in Sec. V B. Furthermore, the analysis above reveals that the ground state in the TBG sector will be of the form of Eq. (3.6). For instance, for $\nu_b = 0$ with $\eta_j^+ = \eta_j^- = (-1)^j$ and $s_j^+ = s_j^- = \uparrow$, $j = 1, 2$, it holds $\tilde{Q}^b_{\boldsymbol{k}} = \tilde{\sigma}_0 \eta_0 s_z$ where $\tilde{Q}^b_{\boldsymbol{k}} = U^* Q^b_{\boldsymbol{k}} U^T$ is the order parameter $Q^b_{\boldsymbol{k}}$ in Eq. (3.13) in the TBG subspace transformed to the chiral basis of Eq. (3.5); in the basis of Eq. (3.11), it holds $Q^b_{\boldsymbol{k}} = \sigma_0 \eta_0 s_z$, which we refer to as the spin-polarized (SP) state. Here and in the following, we use σ_j ($\tilde{\sigma}_j$) to denote Pauli matrices in the band space with index p (in the chiral basis with index c). In addition to the SP state, Eq. (3.6) describes many other possible ground states that are exactly degenerate in the chiral-flat-decoupled limit. A systematic way of seeing this proceeds by noting that the $\mathrm{U}(4) \times \mathrm{U}(4)$ identified [46,61,63] for TBG also persists as a symmetry of MSTG in the chiral-flat-decoupled limit [36]; this immediately follows from the structure of H_{FD} in Eq. (3.1). Here, we refer to this symmetry group as $[\mathrm{U}(4) \times \mathrm{U}(4)]_{b,\mathrm{CF}}$, and its action is particularly simple in the chiral basis [61]

$$\tilde{b}_{\boldsymbol{k}} \rightarrow \mathcal{U} \tilde{b}_{\boldsymbol{k}}, \qquad \mathcal{U} = e^{i \sum_{j=0,3} \sum_{\mu,\mu'=0}^{3} \varphi_{j,\mu,\mu'} \tilde{\sigma}_j \eta_\mu s_{\mu'}}. \quad (3.14)$$

The form of these transformations is readily inferred from Eq. (S48) in the Supplemental Material [59], which indicates that all $\mathcal{U}$ with $[\mathcal{U}, \tilde{\sigma}_3] = 0$ will leave H_{FD} invariant. Under Eq. (3.14), the order parameter defined above transforms as $\tilde{Q}^b_{\boldsymbol{k}} \rightarrow \mathcal{U}^* \tilde{Q}^b_{\boldsymbol{k}} \mathcal{U}^T$, which allows us to generate the entire (continuous) set of exactly degenerate ground states from one “seed” state, such as the SP state, $\tilde{Q}^b_{\boldsymbol{k}} = \tilde{\sigma}_0 \eta_0 s_z$. Since this seed state and $\mathcal{U}$ commute with $\tilde{\sigma}_3$, we know that $[\tilde{Q}^b_{\boldsymbol{k}}, \tilde{\sigma}_3] = 0$ for all ground states. Further noting that $(\tilde{Q}^b_{\boldsymbol{k}})^2 = \mathbb{1}$ (physically related to the Slater-determinant nature), we can thus summarize the properties in the original basis as

$$\begin{aligned} Q^b_{\boldsymbol{k}} &= Q^b, \qquad & [Q^b, \sigma_2] &= 0, \\ (Q^b)^2 &= \mathbb{1}, \qquad & \mathrm{tr}[Q^b] &= 0 \end{aligned} \quad (3.15)$$

at charge neutrality.

The actual Hamiltonian of MSTG is not in the chiral-flat-decoupled limit and does not exhibit an exact $[\mathrm{U}(4) \times \mathrm{U}(4)]_{b,\mathrm{CF}}$ symmetry. Intuitively, this can be thought of as generating an easy axis in this multidimensional space of degenerate states, favoring a specific (subspace of) state(s) in Eq. (3.15). While energetics is required to decide which phase is ultimately preferred by the system—the aim of the subsequent sections—we can use symmetries to derive the discrete and finite set of possible “candidate states”: To this end, we impose only $\mathrm{U}(1)_v$ and global spin rotations $\mathrm{SU}(2)_s$ as exact continuous symmetries. We then know that the candidate order parameters must transform under the irreducible representations of these symmetry groups (and be even or odd under the exact discrete symmetries C_{2z} and Θ), leading to the 11 options listed in Table II. In order to connect smoothly to the limit $D_0 \rightarrow 0$, here we take $Q^g_{\boldsymbol{k}} = -\sigma_z$ in the graphene subspace but emphasize that these order parameters are used only to define the different states and characterize their symmetries. For our numerical and analytical discussion below, they are taken to be only the starting point, and we allow for (and also find) mixing between the TBG-like and graphenelike sectors when $D_0 \neq 0$ as well as momentum dependence in $Q_{\boldsymbol{k}}$.

Finally, we point out that the model introduced in Sec. II, and in which we study energetics below, has an exact $\mathrm{SU}(2)_+ \times \mathrm{SU}(2)_-$ symmetry. Therefore, certain pairs of states, which we call Hund’s partners following Ref. [27], have to be exactly degenerate; see Table II. As we noted earlier, in the realistic system, there is a nonzero intervalley Hund’s coupling $J_H \neq 0$, which will break $\mathrm{SU}(2)_+ \times \mathrm{SU}(2)_-$ down to $\mathrm{SU}(2)_s$, albeit weakly, and favor one member of each of the pairs over the other. For most of the following study, we focus on the $\mathrm{SU}(2)_+ \times \mathrm{SU}(2)_-$ limit, and hence, we can, without loss of generality, restrict the discussion to the first seven states in Table II. However, one has to keep in mind that the real system will realize only one state of each Hund’s pair, which will depend on the (unknown) sign of J_H and precise form of Hund’s coupling

TABLE II. We list the different candidate phases in the TBG-like subspace constructed as the discrete set of states that are part of the large manifold of exact ground states in the chiral-flat-decoupled limit (see Sec. III) but transform under the irreducible representations of the symmetries of the real system. Here, **1** (**3**) is the singlet (triplet) representation of $\mathrm{SU}(2)_s$ and 0 (1) the one (two)-dimensional representation of $\mathrm{U}(1)_v$. For future reference, in Sec. VII we list the behavior (± denoting even and odd, and ✗ indicating absence) under both spinful (Θ_s) and valley ($\tilde{\Theta}$) time-reversal symmetry; see Table I. The last two columns indicate which states are Hund's partners [27], i.e., transform into each other when reversing the sign of Hund's coupling J_H while being exactly degenerate in the $[\mathrm{SU}(2)_+ \times \mathrm{SU}(2)_-]$-symmetric limit, and which sign of J_H favors the respective state.

Type	Short form	Q^b	$\tilde{Q}^b$	$\mathrm{SU}(2)_s$	$U(1)_v$	C_{2z}	$\Theta_s/\tilde{\Theta}$	Hund's partner	J_H
Spin polarized	SP	$\sigma_0\eta_0\boldsymbol{s}$	$\tilde{\sigma}_0\eta_0\boldsymbol{s}$	**3**	0	✓	−/✗	SVP	<0
Valley polarized	VP	$\sigma_0\eta_z s_0$	$\tilde{\sigma}_0\eta_z s_0$	**1**	0	✗	−/−	None	0
Θ-even IVC	IVC_+	$\sigma_0\eta_{x,y} s_0$	$\tilde{\sigma}_0\eta_{x,y} s_0$	**1**	1	✓	+/−	SIVC_+	>0
Θ-odd IVC	IVC_-	$\sigma_y\eta_{x,y} s_0$	$\tilde{\sigma}_z\eta_{x,y} s_0$	**1**	1	✓	−/+	SIVC_-	>0
Θ-odd, sublattice pol. or Hall	SLP_-	$\sigma_y\eta_0 s_0$	$\tilde{\sigma}_z\eta_0 s_0$	**1**	0	✓	−/−	None	0
Θ-even, sublattice pol. or valley Hall	SLP_+	$\sigma_y\eta_z s_0$	$\tilde{\sigma}_z\eta_z s_0$	**1**	0	✗	+/+	None	0
Θ-odd, spin-sublattice-pol. or spin Hall	SSLP_-	$\sigma_y\eta_0\boldsymbol{s}$	$\tilde{\sigma}_z\eta_0\boldsymbol{s}$	**3**	0	✓	+/✗	SSLP_+	<0
Spin-valley polarized	SVP	$\sigma_0\eta_z\boldsymbol{s}$	$\tilde{\sigma}_0\eta_z\boldsymbol{s}$	**3**	0	✗	+/✗	SP	>0
Θ-even, spin-pol. IVC	SIVC_+	$\sigma_0\eta_{x,y}\boldsymbol{s}$	$\tilde{\sigma}_0\eta_{x,y}\boldsymbol{s}$	**3**	1	✓	−/✗	IVC_+	<0
Θ-odd, spin-pol. IVC	SIVC_-	$\sigma_y\eta_{x,y}\boldsymbol{s}$	$\tilde{\sigma}_z\eta_{x,y}\boldsymbol{s}$	**3**	1	✓	+/✗	IVC_-	<0
Θ-even, spin-subl. pol. or spin-valley Hall	SSLP_+	$\sigma_y\eta_z\boldsymbol{s}$	$\tilde{\sigma}_z\eta_z\boldsymbol{s}$	**3**	0	✗	−/✗	SSLP_-	>0

(see the Supplemental Material [59] Sec. F 5 for more details). Taking, for concreteness, the intervalley Hund's coupling to be of the form

$$H_2 = \frac{J_H}{N}\sum_{\boldsymbol{q}} \boldsymbol{S}^+_{\boldsymbol{q}} \cdot \boldsymbol{S}^-_{-\boldsymbol{q}}, \quad \boldsymbol{S}^{\pm}_{\boldsymbol{q}} = \frac{1}{2} c^\dagger_{\boldsymbol{k}+\boldsymbol{q}} (\mathbb{1} \pm \eta_z) c_{\boldsymbol{k}}, \tag{3.16}$$

we can, in the chiral-flat-decoupled limit, uniquely associate a single state of each Hund's pair with a given sign of J_H; this is indicated in the last column in Table II.

IV. HARTREE-FOCK NUMERICS

As it facilitates the presentation of the results, we begin the discussion of correlated phases away from the chiral-flat-decoupled limit with the HF numerics and postpone the complementary analytics to Sec. V. Furthermore, we first focus on the charge-neutrality point $\nu = 0$.

A. Hartree-Fock method

In the HF approximation, one focuses on Slater-determinant states $|\Psi[P_{\boldsymbol{k}}]\rangle$ characterized by the correlation matrix $P_{\boldsymbol{k}}$ as defined in Eq. (3.11). Consequently, it holds $P_{\boldsymbol{k}}^2 = P_{\boldsymbol{k}}$ or, equivalently, $Q_{\boldsymbol{k}}^2 = \mathbb{1}$; this is also true for the exact candidate ground states constructed in Sec. III C for the chiral-flat-decoupled limit, and hence, the HF approximation is expected to provide reliable results.

The goal of our HF numerics is to determine the optimal $Q_{\boldsymbol{k}}$ that yields the lowest-energy expectation value with respect to the interacting Hamiltonian for MSTG introduced in Sec. II. To be more specific, we start from the full Hamiltonian $H = H^{\mathrm{full}}_{0,1} + H^{\mathrm{full}}_{0,2} + H_1$ consisting of the continuum model in Eq. (2.1), the displacement-field term in Eq. (2.4), supplemented by the density-density interaction in Eq. (2.8), and perform a mean-field decoupling. Using the same notation as in Eq. (2.10b), the resulting HF mean-field Hamiltonian reads as

$$\begin{aligned} H^{\mathrm{MF}} = & \sum_{\boldsymbol{k}\in\mathrm{MBZ}} \epsilon_{n,\eta}(\boldsymbol{k}) f^\dagger_{\boldsymbol{k};n,\eta,s} f_{\boldsymbol{k};n,\eta,s} \\ & + \sum_{\boldsymbol{k}\in\mathrm{MBZ}} f^\dagger_{\boldsymbol{k}} [h_H[P](\boldsymbol{k}) + h_F[P](\boldsymbol{k})] f_{\boldsymbol{k}} \\ & - \frac{1}{2} \sum_{\boldsymbol{k}\in\mathrm{MBZ}} \mathrm{Tr}[h_H[P](\boldsymbol{k}) P^T_{\boldsymbol{k}} + h_F[P](\boldsymbol{k}) P^T_{\boldsymbol{k}}], \end{aligned} \tag{4.1}$$

where the Hartree and Fock contributions to the mean-field Hamiltonian can be written in terms of the projector $P_{\boldsymbol{k}}$ as

$$h_H[P](\boldsymbol{k}) = \frac{1}{N} \sum_{\boldsymbol{G}\in\mathrm{RL}} V(\boldsymbol{G}) F_{\boldsymbol{k},\boldsymbol{G}} \sum_{\boldsymbol{k}'\in\mathrm{MBZ}} \mathrm{Tr}[F^*_{\boldsymbol{k}',\boldsymbol{G}} P_{\boldsymbol{k}'}] \tag{4.2}$$

and

$$h_F[P](\boldsymbol{k}) = -\frac{1}{N} \sum_{\boldsymbol{q}} V(\boldsymbol{q}) F^\dagger_{\boldsymbol{k},\boldsymbol{q}} P^T_{\boldsymbol{k}+\boldsymbol{q}} F_{\boldsymbol{k},\boldsymbol{q}}, \tag{4.3}$$

respectively. This form of the HF mean-field Hamiltonian is valid for an arbitrary number of bands kept. In the numerics presented here, we focus on the four bands for each spin and valley flavor that are closest to the Fermi level, which contains the graphenelike and TBG-like bands we focus on in the analytics. We verify for representative values of D_0 and w_0 that the solutions we obtain are stable against doubling the number of remote bands in our self-consistent calculation in the Supplemental Material [59] Sec. C 3.

As pointed out in several HF works on TBG [45–48], it is important to note that the continuum model $H^{\mathrm{full}}_{0,1}$ already references electron-electron interactions in the experimentally determined values for microscopic model parameters, and therefore, we must define a reference subtraction projector P_0 such that interactions will not be double counted in our numerics. Here we choose P_0 such that the projected low-energy Hamiltonian exhibits the manifestly particle-hole-symmetric interaction in Eq. (2.10). As shown in Ref. [61] for TBG, this ansatz has the natural interpretation of effectively taking into account the HF contributions from all remote bands that have been projected out.

To determine the optimal $P_{\boldsymbol{k}}$, we start with an initial guess for it with the symmetries of a given candidate order in Table II. We then use the HF Hamiltonian in Eq. (4.1) to compute a new projector $P_{\boldsymbol{k}}$ and iterate until $P_{\boldsymbol{k}}$ converges. More details on our iterative HF procedure and subtraction point are given in the Supplemental Material [59] Sec. C 2.

B. Band structures

In this section, we discuss the band structures of the self-consistent solutions we find at $D_0 = 0$ for each of the states in Table II and how these band structures evolve as D_0 increases.

1. Self-consistent band structures at $D_0 = 0$

At $D_0 = 0$, we can separately describe the behavior of the graphenelike and TBG-like bands for each type of state, since, for all states we consider, the graphenelike bands near the Fermi level at $D_0 = 0$ do not mix with any other bands near the K and K' points. They have a bandwidth larger than the scale of Coulomb interactions. For this reason, the Dirac cones of the graphenelike bands prefer a $Q^g_{\boldsymbol{k}}$ which equally fills the lower bands of the continuum model and preserves all point-group symmetries for every class of solution we study. The Dirac cones thus remain semimetallic and are, in this sense, "spectators" at $D_0 = 0$, in agreement with Sec. III. On the other hand, the TBG-like bands have a bandwidth (5–10 meV) smaller than the scale of the Coulomb energy at $D_0 = 0$ and therefore become insulating as they are polarized for a given symmetry breaking $P_{\boldsymbol{k}}$.

We find converged solutions for each ansatz in Table II and show representative band structures for those states which have the lowest energy in the leftmost panels of Fig. 3. Additional band structures for solutions not shown in Fig. 3 can be found in the Supplemental Material [59] Sec. C 3. We note the similarity of the IVC_ band structure in the TBG-like bands to the band structure of the ground state in Ref. [46].

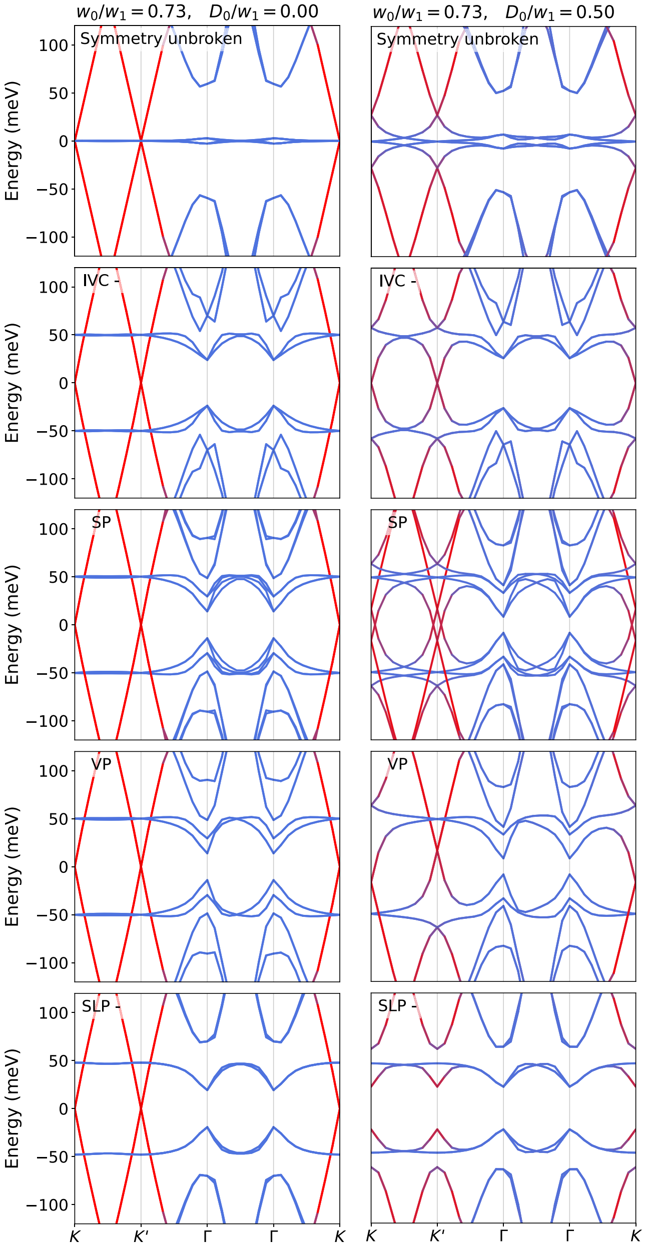

FIG. 3. HF band structures in the limit $D_0 = 0$ (left) and nonzero D_0 (right) as obtained from Eq. (4.1) for the optimal $P_{\boldsymbol{k}}$ in the respective symmetry-breaking channel defined in Table II. We show only the states which are either ground states or subleading energy states for some region of our phase diagram, with a full set of band structures available in the Supplemental Material [59] Sec. C 3. Each band of the HF Hamiltonian is colored according to the expectation value of the mirror-symmetry operator within each band as a function of $\boldsymbol{k}$, with the expectation value ranging from −1 (red) to +1 (blue).

2. Self-consistent band structures for $D_0 > 0$

All the solutions described for $D_0 = 0$ are insulating in the TBG-like bands and semimetallic in the graphenelike bands. However, as D_0 increases and the TBG-like and graphenelike bands begin to hybridize, the graphenelike bands begin to play a more important role.

For the SP and VP states which preserve $C_{2z}\Theta$ and $\mathrm{U}(1)_v$, the hybridized Dirac crossings are protected (and pinned to the K and K' points due to C_{3z}), meaning if the

TBG-like bands acquire a spin or valley polarization, the Dirac crossings of the graphenelike bands must connect to these polarized bands as they are pushed away from the Fermi level. Away from the K points of the MBZ, the graphenelike bands will likely still prefer to fill the lowest bands of the noninteracting model. Therefore, the VP and SP are generically expected to be metallic for $D_0 > 0$. This is indeed what we find, as shown in the right panels for the SP and VP states in Fig. 3.

The band structures of the IVC$_\pm$ states also retain Dirac crossings at the K and K' points for nonzero D_0, as they exhibit C_{3z} and a $\boldsymbol{k}$-local antiunitary symmetry that commutes with C_{3z} (for the IVC$_+$ and IVC$_-$ these are $C_{2z}\Theta$ and $C_{2z}\tilde{\Theta}$, respectively). However, unlike the SP and VP states, the IVC$_\pm$ states also preserve $\mathrm{SU}(2)_s$ and C_{2z}, which pin the Dirac crossings at the Fermi level at $\nu = 0$. We therefore expect the intervalley coherent states will remain semimetallic as D_0 increases. We observe this to be true for the self-consistent solutions, as can be seen in the right IVC$_-$ panel in Fig. 3.

The last class of states is the sublattice-polarized, $C_{2z}\Theta$-symmetry-breaking states (SLP$_\pm$, SSLP$_-$) which preserve $\mathrm{U}(1)_v$. We expect these states will generally be insulating for nonzero D_0 as there are no protected Dirac crossings, and both the TBG-like and graphenelike bands can be gapped out. This is indeed seen in our numerics, with insulating band structures for the SLP$_+$, SLP$_-$, and SSLP$_-$ states. The band structure of the SLP$_-$ state is shown in Fig. 3.

C. Energies and phase diagram

Having established the band structures of the different possible phases, we next turn to their relative energetics and discuss which states are expected to be favored energetically.

The evolution of the energies of each of our self-consistent solutions as a function of w_0 and D_0 is shown in Fig. 5 (see also Supplemental Material [59] Fig. S2). As mentioned before, at $D_0 = 0$, the Hamiltonian of the system is given by the sum of the Hamiltonian of TBG and that of graphene, both with Coulomb interactions, which are further coupled to each other by a density-density interaction. While we construct only exact eigenstates in Sec. III for the chiral-flat-decoupled limit, we expect a similar picture when $w_0, W_{\mathrm{TBG}} \neq 0$: Given that the bandwidth of the graphenelike bands is large compared to the scale of the Coulomb interactions, we expect the graphene bands will prefer to fill the lower bands of the continuum model. As the graphene density of states is small compared to that of the flat bands of TBG, it should not crucially alter the ground state in the TBG sector—at least close to the magic angle. Based on previous work [46,48], we thus expect that the IVC$_-$ state has the lowest energy for $D_0 = 0$ (though with a smaller energy difference than in previous works between our IVC$_-$ and spin-polarized phase due to our choice of subtraction point). Both expectations for the graphenelike and TBG-like bands are confirmed by our numerics which finds the IVC$_-$ state has the lowest energy of all our candidates for all values of w_0 studied in the decoupled limit, $D_0 = 0$. We also recover these observations analytically in Sec. V.

The lowest-energy state for $D_0 \neq 0$ cannot be directly inferred from knowledge of the physics of TBG as a finite D_0 induces hybridization between the TBG-like and graphenelike bands near the K and K' points of the MBZ; it further breaks symmetries in the TBG sector, and hence, changes the basic form of its dispersion and interaction matrix elements (form factors). Consequently, it is not clear whether the ground state in the TBG-like and/or graphenelike sector changes with increasing D_0. As can be seen in Fig. 5 as well as in the corresponding phase diagram in Fig. 4, we find within HF that the IVC$_-$ remains the ground state for an extended range of D_0, which increases with w_0. For reference, the range of D_0 in Figs. 4 and 5 when combined with additional studies at larger D_0 in the Supplemental Material [59] Sec. E corresponds roughly to the range of displacement fields studied experimentally in Ref. [30].

Beyond the critical value of D_0 for the IVC$_-$, the SLP group of states (SLP$_\pm$, SSLP$_-$) dominates. While these latter three states are almost degenerate for all parameters D_0, w_0 studied, there is a slight preference toward the time-reversal-odd SLP$_-$ (quantum Hall), predominantly associated with the Hartree energy. While a SP or VP phase does not appear as a ground state in Fig. 4, we find the

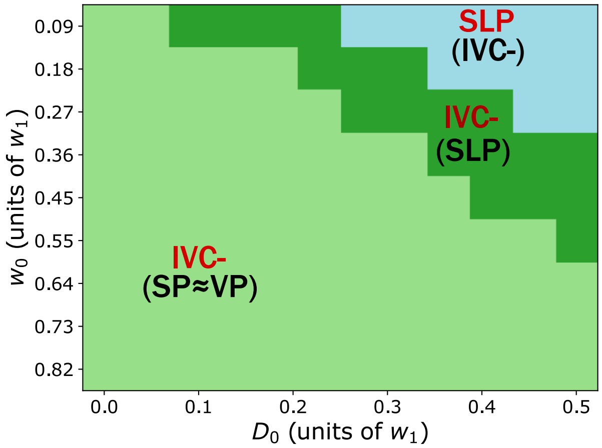

FIG. 4. Phases obtained by self-consistent HF method as a function of w_0 and D_0. Both the leading instability (red) and the subleading ones (black, in parentheses) are shown. The phases are identified by the symmetries they break (see Table II), and representative band structures can be found in Fig. 3. We show only one state as a representative of each pair of Hund's partners which are degenerate in our Hartree-Fock procedure. We label the nearly degenerate SLP$_+$, SLP$_-$, SSLP$_+$, and SSLP$_-$ phases with "SLP," though note the preference in our numerics is for the SLP$_-$ state from a Hartree contribution.

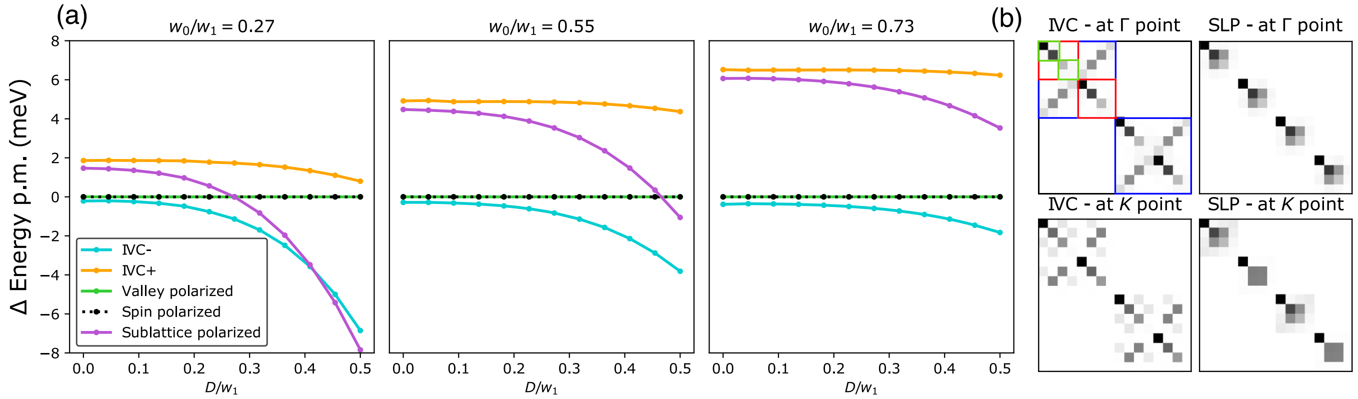

FIG. 5. (a) Line cuts for fixed w_0 showing the energy of our self-consistent solutions relative to a SP state as a function of D_0. We use $w_0 = 124$ meV and four bands per spin and valley, with dielectric constant $\epsilon = 7$ and screening distance $d = 40$ nm. Full energies as a function of w_0 and D_0 can be found in the Supplemental Material [59] Fig. S2. Note that the $\mathrm{SLP}_{\pm}$ and SSLP_{-} are not exactly degenerate, as we discuss in the main text, but are plotted as a single line here since the splitting is too small to be visible on the scale of the plot. (b) Matrix form of our converged IVC_{-} and SLP_{-} orders $P_{\boldsymbol{k}}$ for $\boldsymbol{k}$ near the Γ point and near the K point. The matrix structure of $P_{\boldsymbol{k}}$ is organized such that the largest block outlined in blue denotes spin flavor, the next largest block outlined in red denotes valley flavor, the green block denotes upper and lower bands in the continuum model, and the final two boxes denote the graphenelike and TBG-like band in the upper-band box and the TBG-like then graphenelike bands in the lower-band box.

energetically close SP or VP states are either the second or third lowest energy state to the IVC_{-} and SLP group across the phase diagram. In the next subsection, we recover many of these features analytically by investigating the aforementioned energetic contributions perturbatively.

V. ANALYTICAL PERTURBATION THEORY

Finally, we complement the HF numerics with an analytical study of the behavior of the energies and the order parameters of the degenerate ground states of the chiral-flat-decoupled limit ($w_0 = W_{\mathrm{TBG}} = D_0 = 0$) of Sec. III and Table II when turning on W_{TBG}, D_0, and w_0. We first investigate the ordering tendencies of the graphenelike bands (Sec. V A) and their mixing with the TBG-like bands (Sec. V B), before addressing the energetic contributions coming from the D_0,w_0-induced distortion of the TBG-like form factors (Sec. V C) and band structure (Sec. V D).

A. Ordering in the graphenelike bands

Since the graphene and graphenelike bands in Fig. 2(b) are highly dispersive, starting from a flat-band limit, as is natural for the TBG-like sector, is not possible for the graphene(like) bands. Their bands are coupled, without any band gap, to the TBG-like bands with a high density of states, and thus, treating the interactions between the two subsystems as a perturbation is also not necessarily controlled for realistic parameters. Instead, here we use a different control parameter: Based on the band structure, we expect the effect of the TBG(-like) bands on the graphene(like) bands to be the strongest around the K and K' points and very weak away from it. To formalize this, let us assume that the graphenelike bands remain in their filled-lower-bands state away from the K and K' points but allow them to be "deformed" in the region $\mathcal{A} = \mathcal{A}_+ \cup \mathcal{A}_-$ of the MBZ, where $\mathcal{A}_+$ ($\mathcal{A}_-$) are simply connected and centered on the K (K') point. As explained in detail in the Supplemental Material [59] Sec. F 3, we study the energy of symmetry-allowed ordering tendencies of the graphenelike bands for the different candidate phases in Table II in the limit where the area of $\mathcal{A}$ is small (compared to that of the MBZ).

To illustrate this procedure, let us consider the SP state. Since the TBG-like bands break spin-rotation symmetry, it is natural to assume that the same happens to the graphenelike bands in $\mathcal{A}$; postponing the discussion of mixing between the bands to Sec. V B, this means that $(Q^g_{\boldsymbol{k}})_{\eta,\eta'} = \delta_{\eta,\eta'}\sigma_0 \boldsymbol{s}$, $\boldsymbol{k} \in \mathcal{A}_\eta$, in the notation introduced in Sec. III C, while $(Q^g_{\boldsymbol{k}})_{\eta,\eta'} = -\delta_{\eta,\eta'}\sigma_3$ for all other $\boldsymbol{k}$. Here we already anticipate (as is also readily checked within this formalism) that it is energetically more favorable if only the graphene valley $\eta = +$ ($\eta = -$) that is at low energies in the region $\mathcal{A}_+$ ($\mathcal{A}_-$) exhibits spin polarization. Denoting the linear size of $\mathcal{A}_\pm$ by $\Delta k > 0$, the structure of the energetic change associated with the deformation of the graphene order is asymptotically given by

$$\Delta E \sim d_1 |D_0| (\Delta k)^2 + d_2 (\Delta k)^3 + I_{gg} (\Delta k)^3 - I_{gb} D_0^2 (\Delta k)^2 \tag{5.1}$$

for small Δk and D_0; here, $d_{1,2} > 0$ are positive constants (independent of Δk and D_0, but dependent on w_0) associated with the graphenelike dispersion, while I_{gg} depends on the graphene-graphene form factors F^{gg} and $I_{gb} > 0$ on F^{gb} and F^{gg}. The explicit form and derivation can be found in the Supplemental Material [59] Sec. F 3.

From Eq. (5.1), we can read off the behavior of the graphenelike bands of the SP state. For $D_0 = 0$, we see that $\Delta E > 0$ (deformation is energetically disfavored) as long as $d_2 > I_{gg}$. While this is what our numerics shows, we point out that $d_2 < I_{gg}$ would imply that single-layer graphene spontaneously magnetizes, which is known to be not the case. This agrees with our result in Sec. III based on adiabatically turning on the coupling between the TBG and graphene system and our numerics which displays unpolarized graphene Dirac cones in Fig. 3 at $D_0 = 0$. When $D_0 \neq 0$, we see that the energetic cost coming from the dispersion in the first line of Eq. (5.1) will always overcompensate the energetic gain coming from the scattering between the graphene- and TBG-like bands (at least in a finite range of $D_0 \neq 0$). This is also consistent with our HF numerics: As can be seen in the band structure in Fig. 3, the graphenelike bands are not spin polarized for nonzero D_0 (see also Fig. S11 in the Supplemental Material [59] where $Q_{\boldsymbol{k}}$ as obtained in HF are shown).

In the same way, all the other states in Table II can be analyzed (see the Appendix A 1) with results summarized in Table III. Most importantly, we see that only the SLP$_\pm$ states can benefit from, and hence, develop order in the graphenelike bands.

B. Mixing between the bands

We next look into the mixing between the TBG-like and graphenelike bands. While it is clear by symmetry that the mixing has to vanish for $D_0 = 0$ and be generically present for $D_0 \neq 0$, here we investigate the associated energetic gain and precise form of the band mixing for our candidate states in Table II.

Let us take the IVC$_-$ state as an example. We show in Appendix A 2, that only two different mixing matrices defined as

$$(M^Q_{\boldsymbol{k}})_{(p,\eta,s),(p',\eta',s')} \coloneqq (Q_{\boldsymbol{k}})_{(b,p,\eta,s),(g,p',\eta',s')} \tag{5.2}$$

are possible:

$$M^Q_{\boldsymbol{k}} = 2\sqrt{2}i(\sigma_x P_\pm \pm \sigma_0 \eta^\mp)\varphi_{\boldsymbol{k}}, \qquad \boldsymbol{k} \in \mathcal{A}_\pm \tag{5.3a}$$

and

$$M^Q_{\boldsymbol{k}} = 2\sqrt{2}i(\sigma_z P_\pm \pm i\sigma_y \eta^\mp)\varphi_{\boldsymbol{k}}, \qquad \boldsymbol{k} \in \mathcal{A}_\pm. \tag{5.3b}$$

Here, we define $P_\pm = (\eta_0 \pm \eta_z)/2$ and $\eta^\pm = (\eta_x \pm i\eta_y)/2$. Intuitively, the first mixing matrix means that the lower (upper) graphenelike bands of the valley that is at low energies at K or K' mixes with the upper (lower) and lower (upper) TBG-like bands of the same and opposite valley, respectively. The second option in Eq. (5.3b) describes the "twisted" situation where the lower (upper) graphenelike band mixes with the lower (upper) TBG-like bands of the same valley and the upper (lower) band in the opposite valley. The HF result for $Q_{\boldsymbol{k}}$ close to the K point shown in Fig. 5(b) is consistent with Eq. (5.3a). As we discuss in Appendix A 2, the associated energetic gain is of the form $\Delta E_{gb} \sim -g_3(\Delta k)^2 D_0^2$, where $g_3 > 0$; this is indicated in Table III.

In the same way, all other candidate states can be studied (see Supplemental Material [59] Sec. F 4). In accordance with our expectation based on symmetry, we find no mixing and vanishing energetic gain $\Delta E_{gb} = 0$

TABLE III. Summary of the different energetic contributions, as discussed in Sec. V, for the candidate orders in Table II when tuning away from the chiral-flat-decoupled limit ($w_0 = W_{\text{TBG}} = D_0 = 0$). By construction, the energies are identical for the respective Hund's partners and are hence omitted. Here, $\Delta E_{bb}(W_{\text{TBG}} = 0)$ is the change of energy relative to SP phase coming from the modifications of the form factors in the TBG-like bands when turning on w_0 and D_0 in the flat limit ($W_{\text{TBG}} = 0$). As indicated in the column labeled ΔE_{gg}, only the SLP$_\pm$ states gain energy by ordering in the graphenelike bands immediately when $D_0 \neq 0$. In all cases, $D_0 \neq 0$ leads to mixing between the bands with energetic gain, as listed in the chiral limit $w_0 = 0$ in the column ΔE_{gb}. Here, Δk is the linear size of the fraction $\mathcal{A}_\pm$ of the MBS where ordering in the graphenelike bands and mixing take place. The four columns with $\bar{E}^b_j$ indicate which of the four contributions to the TBG dispersion in Eq. (2.6) can lower the energies to second order in W_{TBG}. Finally, in the last columns, we list the energy change associated with a finite value of Hund's coupling in Eq. (3.16) for the respective state (ΔE_J) and its Hund's partner (ΔE^H_J), if it exists, in the chiral-flat-decoupled limit. All coefficients obey $c_j, g_\pm, g_j, \beta_j > 0$ and explicit expressions can be found in the Supplemental Material [59] Sec. F.

Type	Q^b	$\tilde{Q}^b$	$\Delta E_{bb}(W_{\text{TBG}} = 0)$	ΔE_{gg}	ΔE_{gb}	$\bar{E}^b_0$	$\bar{E}^b_1 w_0$	$\bar{E}^b_2 D_0$	$\bar{E}^b_3 w_0 D_0$	ΔE_J	ΔE^H_J
SP	$\sigma_0\eta_0\boldsymbol{s}$	$\tilde{\sigma}_0\eta_0\boldsymbol{s}$	0 (by definition)	0	$-g_1(\Delta k)^2 D_0^2$	✗	✗	✗	✗	$2J_H\beta_1$	$-2J_H\beta_1$
VP	$\sigma_0\eta_z s_0$	$\tilde{\sigma}_0\eta_z s_0$	0	0	$-g_1(\Delta k)^2 D_0^2$	✗	✗	✗	✗	0	0
IVC$_+$	$\sigma_0\eta_{x,y}$	$\tilde{\sigma}_0\eta_{x,y}$	$c_1 D_0^4 + c_3 w_0^2$	0	$-g_2(\Delta k)^2 D_0^2$	✗	✓	✓	✗	$-3J_H\beta_2$	$J_H\beta_2$
IVC$_-$	$\sigma_y\eta_{x,y}$	$\tilde{\sigma}_z\eta_{x,y}$	$c_1 D_0^4 + c_4 w_0^2 D_0^4$	0	$-g_2(\Delta k)^2 D_0^2$	✓	✓	✗	✗	$-3J_H\beta_2$	$J_H\beta_2$
SLP$_-$	σ_y	$\tilde{\sigma}_z$	$c_3 w_0^2 + c_4 w_0^2 D_0^4$	$-g_-(\Delta k)^2\lvert D_0\rvert^3$	$-g_1(\Delta k)^2 D_0^2$	✓	✗	✓	✗	0	0
SLP$_+$	$\sigma_y\eta_z$	$\tilde{\sigma}_z\eta_z$	$c_2 D_0^4 + c_3 w_0^2 + c_4 w_0^2 D_0^4$	$-g_+(\Delta k)^2\lvert D_0\rvert^3$	$-g_3(\Delta k)^2 D_0^2$	✓	✗	✓	✗	0	0
SSLP$_-$	$\sigma_y s_z$	$\tilde{\sigma}_z s_z$	$c_3 w_0^2 + c_4 w_0^2 D_0^4$	0	$-g_1(\Delta k)^2 D_0^2$	✓	✗	✓	✗	$2J_H\beta_3$	$-2J_H\beta_3$

when $D_0 = 0$, while mixing immediately sets in and $\Delta E_{gb} < 0$ once $D_0 \neq 0$. In all cases, ΔE_{gb} scales as $\Delta E_{gb} \sim -g_j (\Delta k)^2 D_0^2$, $g_j > 0$, as $D_0 \to 0$. While $g_j = g_j(w_0)$ depend on w_0, we list ΔE_{gb} in the chiral limit $w_0 = 0$ in Table III, as it reveals some structure: We see that the energetic gain coming from hybridization is identical for the two IVCs, and it is the same for the four states SP, VP, SLP_-, and SSLP_- in the chiral limit.

To provide a second example, we find a mixing matrix for the SLP_- given by

$$M_{\boldsymbol{k}}^{Q} = 2i(\sigma_y + \sigma_z)P_\pm \varphi_{\boldsymbol{k}}, \qquad \boldsymbol{k} \in \mathcal{A}_\pm. \tag{5.4}$$

This means that there is only mixing in the valley for which the graphenelike bands are at low energies and that both upper and lower graphenelike bands mix with both TBG-like bands. This is consistent with the $Q_{\boldsymbol{k}}$ in Fig. 5(b) that we find for the SLP_- in HF close to the K point.

C. Deforming the form factors

Apart from the mixing with and the "proximity-induced" order in the graphenelike bands, there are also important energetic contributions directly within the TBG-like bands when tuning away from the chiral-flat-decoupled limit. While some of these contributions are analogous to TBG [46,62], others are not: Nonzero D_0 strongly breaks P (see Table I), and hence, induces terms in the TBG-like band structure [see second line in Eq. (2.6)] without any analog in TBG. It also leads to terms in the form factors [see Eq. (S33a) in the Supplemental Material [59] for details] that cannot be present in TBG and have not been studied in the literature.

Here we begin with the impact of the form factors and restrict ourselves for now to the flat limit $W_{\mathrm{TBG}} = 0$. In the column labeled ΔE_{bb} in Table III we show the energy of the candidate states for nonzero w_0 and D_0 relative to the SP (see the Supplemental Material [59] Sec. F 1 for explicit expressions for the prefactors $c_j > 0$). First, for $D_0 = 0$, we recover the previous result [46] that the IVC_- and VP are the only states besides the SP that are not penalized when turning on w_0. Second, we see that this changes once $D_0 \neq 0$: If $w_0 = 0$, it is the SLP group of states that is not suppressed by breaking P with D_0 [65], while both IVCs have increasing energy. When both w_0 and D_0 are simultaneously nonzero, the SLP group is also suppressed (by the exact same amount as the IVC_-) compared to the SP and VP. Algebraically, this is related to the fact that the SP and VP order parameters are the only ones that commute with all form factors once $w_0, D_0 \neq 0$ [cf. Eq. (S33a) in the Supplemental Material [59]].

D. Finite TBG bandwidth

Finally, we take into account the finite bandwidth of the TBG-like bands by doing perturbation theory in W_{TBG} in Eq. (2.5), starting from the product states associated with the candidate orders of Table II. We outline only the results here and refer the interested reader to the Supplemental Material [59] Sec. F 2.

Since the correction to the relative energies of the different candidate orders vanishes to first order in W_{TBG}, we focus on second-order perturbation theory, which, if nonzero, will always lower the energy of the states and can be thought of as "superexchange." We consider the superexchange processes associated with all four terms E_j^b, $j = 0, 1, 2, 3$ in Eq. (2.6) of the TBG-like dispersion; the corresponding energetic gain will scale as W_{TBG}^2/U for $j = 0$, $W_{\mathrm{TBG}}^2 w_0^2/U$ for $j = 1$, $W_{\mathrm{TBG}}^2 D_0^2/U$ for $j = 2$, and $W_{\mathrm{TBG}}^2 w_0^2 D_0^2/U$ for $j = 3$ to leading order in D_0 and w_0, where U is the energy scale associated with occupying a $\boldsymbol{k}$ state of an unoccupied flavor in a given ground state. Which of these four superexchange processes are "active" for the candidate states is listed in Table III. We find that, by virtue of being proportional to the identity in Eq. (2.6), E_3^b does not affect the energy of the states. Furthermore, we see that the displacement-induced superexchange process favors the IVC_+ and the SLP group of states.

E. Comparison of energetics

Taken together, the energetics obtained analytically as summarized in Table III agrees well with the numerics in several aspects: We can see that the energies of the SLP_+, SLP_-, and SSLP_- are expected to be very close, exactly as seen in HF; see Fig. 5. There is a very small splitting among the three associated with the fact that the SSLP_- cannot benefit from ordering in the graphenelike bands, that effect is weaker for the SLP_+ than for the SLP_- (recall $g_- > g_+$ for small w_0), and that the SLP_+ is slightly suppressed by the Hartree term. We see that there is a small energetic preference toward the SLP_- in the numerics as well. In addition, we can also read off from Table III that the SLP group of states should be preferred for small w_0 and large D_0, which is consistently seen in our HF phase diagram in Fig. 4.

Notwithstanding the good agreement between the HF and the analytics concerning the graphene ordering, mixing between the bands, and the energetics, there are also differences. These differences can be traced back to the additional presence of remote bands, in particular, the bands with σ_h eigenvalues $+1$ just above (below) the almost-flat TBG-like band $p = +$ ($p = -$) away from the K and K' points. While these remote bands are included in our HF numerics, they are not taken into account in the analytics. Most notably, we see that mixing between these bands and the almost-flat TBG-like bands further lowers the energy of IVC_- state relative to the SP and VP states.

F. Breaking $\mathbf{SU(2)_+ \times SU(2)_-}$

Finally, we come back to the fact that certain Hund's partners of states are degenerate in the model we have focused on so far and defined in Sec. II; this can be traced back to the presence of the $\mathrm{SU}(2)_+ \times \mathrm{SU}(2)_-$ spin symmetry. Turning on a finite Hund's coupling $J_H \neq 0$ will lift this degeneracy and also slightly affect the relative energetics of the candidate states. For the form of Hund's coupling defined in Eq. (3.16), we compute the respective change of energy. With more general and explicit expressions available in the Supplemental Material [59] Sec. F 5, we present their impact on the energies of the states in the last two columns of Table III in the chiral-flat-decoupled limit. Here, β_j are positive constants obeying $\beta_2 > \beta_1, \beta_3$. While estimates based on the Coulomb interaction yield an energy change (per unit cell) of $2J_H\beta_1 \simeq -0.2$ meV for the SP state in TBG [66], its actual effective value might be smaller due to screening processes and additional electron-phonon coupling, which can also change the sign of J_H. However, irrespective of the sign of J_H and its precise magnitude, we see that it will favor the $\mathrm{SSLP}_\pm$ states in the otherwise almost-degenerate SLP group of states, since the $\mathrm{SLP}_\pm$ cannot lower their energy with $J_H \neq 0$. This is due to the fact that $\mathrm{SLP}_\pm$ are their own Hund's partners. Similarly, the SP and SVP states will be favored over the VP phase. Finally, we note that the energetic gain coming from J_H is of the same order of magnitude (even larger) for the SIVC_- (IVC_-) compared to the SP (SVP) state. Consequently, we do not expect that J_H will change the fact that the IVC_- dominates over the SP in the phase diagram in Fig. 4.

VI. NUMERICS FOR $\nu = \pm 2$

In this section, we discuss the numerical results for correlated states at half filling of the lower or upper TBG-like bands $\nu = \pm 2$. As we see in Sec. VII below, the normal-state behavior at these fillings is crucial for our understanding of superconductivity in MSTG.

A. Procedure and results

We find self-consistent HF solutions with energies lower than the symmetry-unbroken normal state where, at $D_0 = 0$ ($D_0 \neq 0$), the TBG (TBG-like and graphenelike) bands are spin polarized and, on top of this, exhibit any of the candidate orders defined for $\nu = 0$ in Table II. The obtained spin polarization is our explanation for the observed [30,31] reduced flavor degeneracy setting in around $|\nu| = 2$. We justify choosing spin polarization to reduce the degeneracy at $|\nu| = 2$ by noting that of the options for flavor polarization (spin or valley polarization), only the spin-polarized state has a distinct Hund's partner (the spin-valley-polarized state), meaning that either the spin-polarized state or its Hund's partner will have a lower energy than the valley-polarized state in the presence of nonzero Hund's coupling.

To be more explicit, our self-consistent solutions are found by starting, say, for $\nu = -2$, from a correlator $P^b_{\nu=-2} = \frac{1}{2}(\mathbb{1} + s_z)\frac{1}{2}(\mathbb{1} + Q^b)$ in the TBG-like subspace, where Q^b is any of the candidate orders in Table II; the initial correlator for the graphenelike sector is taken to be filled lower bands of the continuum model at charge neutrality, $P^g = \frac{1}{2}(\mathbb{1} - \sigma_z)$. The corresponding correlator at $\nu = +2$ in the TBG-like sector is simply given by $P^b_{\nu=+2} = \mathbb{1}_{8\times 8} - P^b_{\nu=-2}$. We apply the same iterative procedure as for $\nu = 0$ to obtain self-consistent solutions, with the additional implementation of a chemical potential which is adjusted to fix the filling at $\nu = +2$. As at $\nu = 0$, we allow for solutions with arbitrary momentum-dependent bands, including metallic, semimetallic, and insulating solutions.

We show the band structures resulting from our self-consistent calculation for the spin-polarized IVC_- and spin-polarized SLP states in Fig. 6. The energies we obtain up to $D_0/w_1 = 0.5$ are shown in the Supplemental Material [59] Sec. D, but are qualitatively similar to the numerical energies we compute at $\nu = 0$; we note though, the spin-valley-polarized and spin-polarized IVC_- are closer in energy at $\nu = 2$ than the SVP and IVC_- state at $\nu = 0$. As can be seen in Fig. 6, the graphene bands at $D_0 = 0$ remain unpolarized, in agreement with the analytics in Sec. III. Once a finite displacement field is applied, also the graphenelike bands develop some small polarization. However, exactly as for $\nu = 0$, the Dirac cones of the IVC_- state are not gapped out. We note the IVC_-, which was semimetallic at $\nu = 0$, is metallic at $\nu = \pm 2$ (albeit with small Fermi surfaces). This follows from the additional spin polarization at $|\nu| = 2$, breaking $\mathrm{SU}(2)_s$ which guaranteed its semimetallic character at $\nu = 0$. In Figs. 6(a) and 6(b), we see that the SLP state, which was insulating at $\nu = 0$, becomes semimetallic at $|\nu| = 2$, since the spin

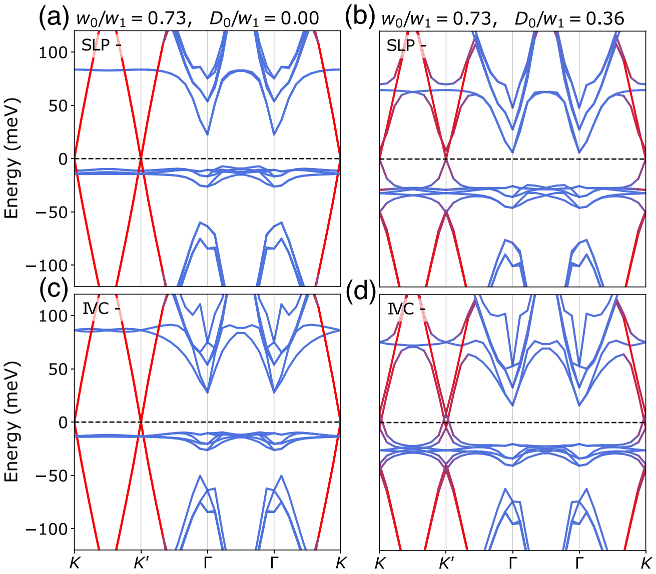

FIG. 6. HF band structures at $\nu = 2$ for the spin-polarized SLP_- state (a) at $D_0 = 0$ and (b) $D_0 > 0$ and spin-polarized IVC_- state (c) at $D_0 = 0$ and (d) $D_0 > 0$.

polarization of the TBG-like bands allows only for SLP order in one of the spin species of the graphenelike bands.

B. Connection to experiment

An important feature in the experimental data on MSTG [30,31], which may be related to our numerics, is the observation of enhanced resistivity at $\nu = 0$ for both $D_0 = 0$ and $D_0 > 0$ and a state with high resistivity observed only at a finite value of D_0 at $\nu = 2$. Taking our results for band structures at $\nu = 0$ and $|\nu| = 2$ together, we note that at $\nu = 0$, the leading phase in our numerics is either a semimetallic IVC$_-$ state or an insulating SLP state, both of which may be compatible with the observed high-resistivity state at $\nu = 0$. At $\nu = 2$, we find our leading solution is a metallic IVC$_-$ state for small values of D_0 and a semimetallic SLP state for large enough D_0—a possible explanation for why high resistivity at $|\nu| = 2$ sets in only above a finite value of D_0 in experiment.

Another notable experimental observation is that the reset of the band structure at $|\nu| = 2$ splits into a Dirac-like feature at $|\nu| = 2$ and a van Hove singularity, associated with a rapid increase and sign change in the Hall density, at $|\nu| = 2 - \delta(D_0)$, $\delta(D_0) \ll 1$ [30]. If we assume that the spin polarization we find persists for a finite range of $|\nu|$ below 2, the band structures in Fig. 6 provide a natural explanation: Lowering the chemical potential, e.g., in Fig. 6(d), until it hits the lower, almost-flat set of bands will lead to a Lifshitz transition where the hole pockets around the K and K' points merge. This could explain the observed behavior of the Hall density. We note that the tendency, visible in Fig. 6, that increasing D_0 pushes these almost-flat bands away from the Fermi level at $|\nu| = 2$, is consistent with this feature being visible only at nonzero D_0 and the associated $\delta(D_0)$ increasing with $|D_0|$ in experiment [30]. The numerical results for larger values of D_0 are discussed in the Supplemental Material [59] Sec. E.

Finally, experimental samples of graphene moiré systems typically exhibit finite heterostrain, and the assumed C_3 symmetry in our analysis is only an approximate symmetry. While sufficiently strong heterostrain can stabilize other phases [67,68], weak strain will not lead to qualitative changes in the phase diagram in Fig. 4 or affect which of our states is metallic, semimetallic, or insulating.

VII. SUPERCONDUCTIVITY

Having established the nature of the correlated phases in MSTG at various filling fractions, we next study the consequences for the superconducting states.

A. Pairing in the presence of polarization

Let us begin with the range of electron filling $2 < |\nu| < 3$, where superconductivity is most prominently observed in experiment [30–32]. We see in Sec. VI that spin polarization supplemented with IVC$_-$ order is favored for realistic parameters at $|\nu| = 2$. Because the associated reduction of the number of flavors in the normal state is seen in experiment over the entire or most of the superconducting range of ν, we assume that spin polarization and superconductivity coexist at least in part of the phase diagram. As follows from the analysis in Ref. [27], where a classification of pairing in almost $[\mathrm{SU}(2)_+ \times \mathrm{SU}(2)_-]$-symmetric graphene moiré systems in the presence and absence of flavor polarization can be found, the superconducting state has to be in a nonunitary triplet phase, irrespective of the precise pairing mechanism. We emphasize that this also holds if the additional IVC$_-$ ordering found in the HF at $|\nu| = 2$ coexists with superconductivity in a finite range of ν: The bands above the Fermi level in the IVC$_-$ band structure in Fig. 6 still exhibit Kramers partners at momenta $\boldsymbol{k}$ and $-\boldsymbol{k}$ with the same spin, due to the preserved spinless $\tilde{\Theta}$ symmetry; these degenerate states can form Cooper pairs with a nonunitary triplet vector. Note that this would not be the case, e.g., for the VP state (shown in Fig. S7 of the Supplemental Material [59]), which does not exhibit exactly degenerate energy levels at $\boldsymbol{k}$ and $-\boldsymbol{k}$ above the Fermi level. Given the strong tendency of MSTG toward superconductivity, this VP phase is thus a less natural candidate order. Indeed, we find it to be subleading in our HF numerics; see Sec. VI.

It is important to note, however, that the spin polarization (and additional IVC$_-$ state) is realized only for $J_H < 0$. While this is expected to be the case if J_H stems entirely from the Coulomb interaction, its sign is unknown. For $J_H > 0$, we would instead obtain the SVP phase with additional SIVC$_-$ order (cf. Table II). In that case, the associated superconductor would also be the corresponding Hund's partner, which is an admixture between a singlet and unitary triplet [27]. In the presence of a magnetic field there is a crucial difference between the two scenarios: While for $J_H < 0$, the SP will just align with the Zeeman field and the superconductor will remain a nonunitary triplet, the two antiparallel spin polarizations in the two valleys of the SVP state will be canted gradually. A coexisting singlet-unitary-triplet superconductor will continuously transition into a nonunitary triplet [27]. For completeness, we demonstrate this explicitly in the Supplemental Material [59] Sec. G 2. Based on the estimate $J_H \lesssim 0.2$ meV [66], we obtain 3 T as the characteristic magnetic field strength of the transition.

B. Pairing without polarization

In experiment [30–32], there are also regions of ν and D_0 with superconductivity but without any signs of flavor polarization in the corresponding normal state (SC II in Fig. 1). Here we discuss the nature and origin of these superconducting phases.

In light of recent experiments in TBG [51–53], which indicate that electron-phonon coupling plays an important role for pairing in graphene moiré systems, the picture proposed in Ref. [54] provides a very promising microscopic scenario: While electron-phonon coupling is likely important to stabilize superconductivity and crucially determines the critical temperature, it might predominantly mediate an $[\mathrm{SU}(2)_+ \times \mathrm{SU}(2)_-]$-symmetric pairing interaction. This symmetry of the pairing mechanism leads to the near degeneracy of singlet and triplet pairing. In the additional presence of flavor polarization, its structure determines whether singlet or triplet is realized, as we discuss above. In the absence of polarization, electron-phonon coupling by itself can never favor triplet over singlet and at most make the two degenerate [69,70]; however, additional Cooper-channel interactions coming from the fluctuation of particle-hole orders can determine whether the superconductor will be in a singlet or triplet state [54]. To analyze this, we consider the action

$$\mathcal{S} = \mathcal{S}_0 + \mathcal{S}_\phi + \mathcal{S}_{\phi f} + \mathcal{S}_{\text{phonon}}, \tag{7.1}$$

which consists of the bare noninteracting action $\mathcal{S}_0$ associated with H_0 in Eq. (2.5) and $\mathcal{S}_\phi$ given by

$$\mathcal{S}_\phi = \frac{1}{2}\int_q \phi_q^j [\chi^{-1}(i\Omega_n, \boldsymbol{q})]_{j,j'} \phi_{-q}^{j'}, \tag{7.2}$$

where ϕ_q^j is the set of real bosonic fields (labeled by j) describing the fluctuations of a given candidate particle-hole order in Table II. We use $q = (i\Omega_n, \boldsymbol{q})$ labeling bosonic Matsubara frequencies Ω_n and momentum $\boldsymbol{q}$, introduce the shortcut $\int_q \ldots \equiv T\sum_{\Omega_n}\sum_{\boldsymbol{q}}\ldots$, and denote the (fully renormalized, low-energy) susceptibility in the particle-hole channel under consideration by $\chi(i\Omega_n, \boldsymbol{q})$. The bosons ϕ_q^j are coupled to the low-energy electron fields $f_{k;n,\eta,s}$, with $k = (i\omega_n, \boldsymbol{k})$ via

$$\mathcal{S}_{\phi f} = \int_q \int_k f_{k+q}^\dagger \lambda^j(\boldsymbol{k}+\boldsymbol{q}, \boldsymbol{k}) f_k \phi_q^j. \tag{7.3}$$

Note that the coupling vertex $\lambda^j(\boldsymbol{k}+\boldsymbol{q}, \boldsymbol{k})$ is in general a matrix in valley, spin, and band space. For instance, a minimal description of fluctuations of the IVC$_-$ state is given by the two-component boson ϕ_q^j, $j = x, y$, with $[\chi(i\Omega_n, \boldsymbol{q})]_{j,j'} \propto \delta_{j,j'}/(\Omega_n^2 + c^2\boldsymbol{q}^2 + \xi^{-2})$, where the coherence length ξ parametrizes the proximity to the critical point. Furthermore, $\lambda^j(\boldsymbol{k}, \boldsymbol{k}') = s_0 \eta_j f_{\boldsymbol{k},\boldsymbol{k}'}$, where $f_{\boldsymbol{k},\boldsymbol{k}'}$ is a matrix in band space ($p = \pm$, $t = b$, g) only, which obeys $f_{\boldsymbol{k},\boldsymbol{k}'} = f_{\boldsymbol{k}',\boldsymbol{k}}^\dagger = -f_{\boldsymbol{k}',\boldsymbol{k}}^T$ due to Hermiticity and ΘC_{2z} symmetry. Finally, the last part $\mathcal{S}_{\text{phonon}}$ in Eq. (7.1) stands for the action of the phonons and their coupling to the electrons.

We integrate out the bosonic modes ϕ_q^j in the action of Eq. (7.1), leading to an interaction between the fermions f. In the saddle-point equations of the Cooper channel, this interaction can be viewed as an $[\mathrm{SU}(2)_+ \times \mathrm{SU}(2)_-]$-symmetry-breaking correction to the $[\mathrm{SU}(2)_+ \times \mathrm{SU}(2)_-]$-symmetric interaction coming from the phonons in $\mathcal{S}_{\text{phonon}}$.

As shown in Ref. [54], whether this symmetry breaking tips the balance toward singlet or triplet is determined by the behavior of the fluctuating modes ϕ_q^j under *spinful* time reversal Θ_s: If the bosonic mode is even (odd) under Θ_s, as indicated by $+$ ($-$) in the column Θ_s in Table II, it will generically favor singlet (triplet) over triplet (singlet) pairing; in the presence of fine-tuning or additional symmetries, the two might remain degenerate. We emphasize that this conclusion does not depend on microscopic details such the precise form of χ in Eq. (7.2) or of λ^j in Eq. (7.3). Because of $\mathrm{U}(1)_v$ symmetry, the system also exhibits the spinless time-reversal symmetry $\tilde{\Theta}$; see Table I. We generalize the analysis of Ref. [54] in the Supplemental Material [59] Sec. G to also include this form of time-reversal symmetry and prove that any ϕ_q^j that is even (odd) under $\tilde{\Theta}$ will generically favor triplet (singlet). This also implies that any ϕ_q^j which has the same behavior under Θ_s and $\tilde{\Theta}$ will keep singlet and triplet degenerate. As expected, this is precisely the case for all order parameters in Table II that are their own Hund's partner.

First, we focus on the superconducting domes (indicated by SC II in Fig. 1) that emerge just outside of the region with flavor polarization and reconstructed band structure [30]. As we mention above, with Coulomb interactions only, the IVC$_-$ order with additional spin polarization is favored over Hund's partner, the SIVC$_-$ with additional SVP order. We can read off from Table II that triplet will then be favored over singlet pairing. As shown in Ref. [27], the resulting triplet will be unitary within mean-field theory but can become nonunitary when spin fluctuation corrections become significant. These two scenarios can be distinguished experimentally since the unitary triplet will exhibit a Berezinskii–Kosterlitz–Thouless transition (of a charge-$4e$, spin-rotation-invariant order parameter combination), while the nonunitary state will not. For the other sign of J_H, singlet pairing (if mean-field theory applies) or a mixed singlet-triplet phase (if the SVP fluctuations dominate) will be realized [27].

Second, we also comment on possible pairing phases close to charge neutrality, although these have not been seen experimentally. For the same sign $J_H < 0$ that favors SP at $\nu = 2$, we obtain the SIVC$_-$ at $\nu = 0$ as the dominant, semimetallic instability at small D_0 and large w_0; see Fig. 4. As can be seen from Table II, it is even under Θ_s and will hence favor singlet pairing. Among the SLP group of states realized for larger D_0, only fluctuations of the SSLP$_\pm$ states will break the $\mathrm{SU}(2)_+ \times \mathrm{SU}(2)_-$ symmetry; the SSLP$_-$ realized for $J_H < 0$ will also favor singlet.

Finally, if electron-phonon coupling does not play any role for pairing in MSTG, i.e., the term $\mathcal{S}_{\text{phonon}}$ in Eq. (7.1) can be neglected, we still obtain the same results (see the Supplemental Material [59] Sec. G 1 for a derivation): If ϕ_q^j are even or odd (odd or even) under Θ_s ($\tilde{\Theta}$), singlet or triplet pairing will be favored. Consequently, the above statements about the singlet-triplet competition still apply in this scenario as well.

C. Relevance of Dirac cones and topology

Motivated by recent theoretical works [25,55,71] discussing the potential importance of WZW terms for superconductivity and insulating behavior in TBG, here we analyze under which conditions this can also be relevant for MSTG. We note that the WZW term is a purely kinematic term associating a Berry phase with spatiotemporal textures of the orders defined on the TBG-like bands, and is *independent* of the interactions between the electrons in these bands. The presence of such a topological term has crucial consequences for direct transitions between superconductivity and correlated insulators, without closing a single-particle gap at integer fillings. We explain in the Supplemental Material [59] Sec. H how the following results can be formally derived from the exhaustive classification of WZW physics in TBG in Ref. [25] and focus here on the main picture and implications.

Although the main superconducting phase is found between $|\nu| = 2$ and $|\nu| = 3$ in experiment [30–32], we begin our analysis at the charge-neutrality point $\nu = 0$ with associated superconducting phase labeled SC III in Fig. 1. Since we expect superconductivity to survive finite displacement fields, we focus on Dirac cones that remain close to the Fermi level for $D_0 \neq 0$. Inspection of the band structure in Fig. 2(b) reveals that the effect of D_0 is to push the two Dirac cones of the graphene and TBG bands of valley $\eta = +$ ($\eta = -$) at K (K') away from the Fermi level, leaving only a single TBG-like Dirac cone of valley $\eta = -$ ($\eta = +$) at low energies. Denoting the fermionic fields by $\psi_{\boldsymbol{q}}$ of these two Dirac cones (per spin), their Hamiltonian reads as

$$H_0^D = \sum_{\boldsymbol{q}} \psi_{\boldsymbol{q}}^\dagger [\rho_x \mu_z s_0 q_x + \rho_y s_0 q_y] \psi_{\boldsymbol{q}}, \tag{7.4}$$

where $\boldsymbol{q}$ is the momentum measured relative to the K (K') point for the Dirac cone at “minivalley” $\mu_z = +$ ($\mu_z = -$). Furthermore, ρ_j are Pauli matrices acting in the Dirac space, which are related to the band-space matrices σ_j used above. In this notation, C_{2z} and (antiunitary) spinful time reversal act as $C_{2z}: \psi_{\boldsymbol{q}} \to \rho_x \mu_x \psi_{-\boldsymbol{q}}$ and $\Theta_s: \psi_{\boldsymbol{q}} \to T \psi_{-\boldsymbol{q}}$, $T = s_y \mu_x$, respectively.

Similar to Ref. [25], we ask what different types of particle-hole orders m_j and superconducting order parameters Δ coupling to $\psi_{\boldsymbol{q}}$ as

$$H_1^D = \sum_{\boldsymbol{q},j} \psi_{\boldsymbol{q}}^\dagger m_j \psi_{\boldsymbol{q}} + \sum_{\boldsymbol{q}} (\psi_{\boldsymbol{q}}^\dagger \Delta T \psi_{-\boldsymbol{q}}^\dagger + \text{H.c.}) \tag{7.5}$$

can form WZW terms. The Hamiltonian $H_0^D + H_1^D$ is equivalent to the low-energy Dirac Hamiltonian for TBG projected into a valley-minivalley-locked subspace, meaning that all pairings and insulating orders with WZW derived in Ref. [25] which survive projection to the same subspace will also be viable in MSTG. This projection is also the reason why the number of possible WZW terms we find here is significantly reduced as compared to Ref. [25].

Based on our analysis of particle-hole instabilities, the Dirac cones in Eq. (7.4) can either be those of the noninteracting bands or those of our leading instability at small D_0—the semimetallic IVC$_-$ state with band structure shown in Fig. 3—which could persist for an extended range of $|\nu| > 0$. The resulting WZW terms we discuss next are identical in both scenarios.

Because of spin-rotation invariance, triplet pairing is not consistent with a WZW term [25]. We find that singlet pairing $\Delta = \rho_0 \mu_0 s_0$, which transforms under the irreducible representation A of the point group, is the only possible superconducting state with a WZW term at $\nu = 0$. This is consistent with the singlet we establish in Sec. VII B near $\nu = 0$ due to electron-phonon coupling and particle-hole fluctuations. Considering all possible compatible insulating orders m_j, we find there are two types: a spin Hall order of the form $\mu_z \rho_z s_{x,y,z}$, which aligns with our SSLP$_-$ order in Table II, and a moiré density wave (MDW) state $\rho_x \mu_{x,y}$, which breaks translations on the moiré lattice scale together with an SLP$_+$ state (ρ_z); see Table IV. We note that since this order is defined in the minivalley-valley-locked space and, in the full space of MSTG, thus also breaks $\mathrm{U}(1)_v$ symmetry in the same way as our IVC states. Interestingly, the SSLP$_-$ is precisely our leading instability for larger D_0 and, hence, constitutes indeed a natural candidate m_j. The MDW state goes beyond our analysis in this work, as we do not consider states which break moiré translational symmetry. We leave this for future work.

At $|\nu| = 2$, the situation is more complicated because the entire band structure is reconstructed as a consequence of interaction-induced flavor polarization. Nonetheless, we expect the low-energy Dirac theory to be still of the form of Eq. (7.4). While there are other possible microscopic realizations, this is true for our leading instability of the SP (or SVP) with additional IVC$_-$ (or SIVC$_-$) order with band structure in Figs. 6(c) and 6(d). Neglecting the small-D_0-induced SP (or SVP) in the graphenelike bands, Eq. (7.4) still applies.

As summarized in Table IV, all options for insulators with singlet pairing then carry over to $|\nu| = 2$. A difference between the two cases is the broken $\mathrm{SU}(2)_s$ spin symmetry, which also allows for triplet pairing. In this case, there are two additional options compatible with the unitary triplet $\Delta = \mu_z s_z$: one set with insulating orders $\rho_z s_{x,y}$ and $\rho_z \mu_z s_z$ and another set with $\rho_x s_z \mu_{x,y}$ and ρ_z. The first two orders correspond to our SSLP$_+$ and SSLP$_-$, respectively. The second two states are a spin-polarized MDW state and the SLP$_+$ state. We find no nonunitary state to be consistent with WZW terms. Since only either singlet or unitary triplet

TABLE IV. Possible particle-hole m_j and superconducting order parameters Δ that can exhibit mutual WZW terms at the indicated filling fractions $\nu = 0$ and $|\nu| = 2$. Here we use the Dirac notation of Eqs. (7.4) and (7.5). As in Ref. [25], moiré density wave (MDW) indicates that the state breaks moiré translational symmetry; A and B refer to the irreducible representations of the point group C_6 of the superconductor (SC). The MDW with singlet pairing row below corresponds to the first row of Table IV in Ref. [25], while the MDW with triplet SC corresponds to the first row of Table VII (or more explicitly, in lines 5 and 9 of Table XV).

$\lvert\nu\rvert$	m_j	Type	Δ	SC type
0,2	$\mu_z\rho_z\boldsymbol{s}$	SSLP$_-$	$\mathbb{1}$	A singlet
0,2	$\rho_x(\mu_x, \mu_y); \rho_z$	MDW; SLP$_+$	$\mathbb{1}$	A singlet
2	$\rho_z(s_x, s_y); \rho_z\mu_z s_z$	SSLP$_+$/SSLP$_-$	$\mu_z s_z$	B unit. triplet
2	$\rho_x s_z(\mu_x, \mu_y); \rho_z$	MDW/SLP$_+$	$\mu_z s_z$	B unit. triplet

are possible, the underlying flavor polarization of the TBG-like bands in Figs. 3(c) and 3(d)must be SVP rather than SP. Consequently, the WZW terms at $|\nu| = 2$ are more likely relevant if $J_H > 0$.

VIII. CONCLUSION AND DISCUSSION

To summarize, we study particle-hole instabilities and superconductivity in MSTG for different filling fractions ν and displacement-field values D_0, using a combination of analytical arguments and HF numerics. We start in Sec. III in the limit $D_0 = 0$, where the noninteracting band structure is just given by the spectrum of TBG and single-layer graphene. In the interacting Hamiltonian (3.1), these two subsystems are coupled by the density-density interaction in Eq. (3.4). We show that states of the form $|\Psi^g_j(\nu_b)\rangle|\Psi^b_0(\nu_b)\rangle$, where $|\Psi^g_j(\nu_b)\rangle$ are the correlated semimetallic eigenstates of single-layer graphene and $|\Psi^b_0(\nu_b)\rangle$ are the eigenstates [62] in Eq. (3.6) of the TBG Hamiltonian in the flat limit, are also exact eigenstates of the MSTG in Eq. (3.1). Furthermore, if $|\Psi^b_0(\nu_b)\rangle$ are ground states of the TBG Hamiltonian, $|\Psi^g_j(\nu_b)\rangle|\Psi^b_0(\nu_b)\rangle$ are shown to be exact ground states of MSTG for a finite range of the coupling strength quantified by λ in Eq. (3.4) between the two sectors. In this sense, not only the bare band structure but also the *interacting* physics of MSTG can be separated into that of single-layer graphene and TBG in the flat-decoupled limit.

We use these results to construct the set of candidate particle-hole orders summarized in Table II, which are exactly degenerate in the chiral-flat-decoupled limit [defined by further setting $w_0 = 0$ in Eq. (2.3)]. We take these states as our starting point of the HF numerics and analytical perturbation theory, which are not based on λ being small and allow to tune away from the chiral-flat-decoupled limit. The resulting band structures for $\nu = 0$ of the most important candidate orders are shown in Fig. 3 for zero and nonzero D_0, with w_0 close to what is believed to describe the real system [56,57] and finite TBG bandwidth. We see three distinct types of behavior with different experimental signatures when turning on D_0: The IVC$_\pm$ and their Hund's partners SIVC$_\pm$ retain their semimetallic behavior for $D_0 \neq 0$, while the graphene Dirac cones of the SLP$_\pm$ and SSLP$_-$ (and its Hund's partner SSLP$_+$) are gapped out when turning on D_0. Interestingly, for the VP and SP (and its Hund's partner SVP), a finite D_0 induces small Fermi surfaces. In combination with further transport and, in particular, scanning tunneling microscopy experiments, which are sensitive to the local spectrum of the system, the computed spectra could help shed light on the correlated physics of MSTG.

The relative energetics between these candidate states as a function of D_0, w_0, and the TBG bandwidth is very rich: As summarized in Table III, there are many contributions without any analog in TBG—the mixing between the TBG and graphene bands, additional ordering in the graphene bands, and the D_0-induced breaking of symmetries in the TBG sector, which changes interaction matrix elements and induces new superexchange processes. The resultant phase diagram in the $D_0 - w_0$ plane with leading and subleading phases is presented in Fig. 4: At small D_0, a semimetallic intervalley coherent phase is favored, which transitions into a sublattice-polarized phase at larger D_0. Among the latter set of states, we expect the SSLP$_\pm$ to dominate as they are the only states in this otherwise almost-degenerate manifold that can benefit from the intervalley Hund's coupling J_H in Eq. (3.16).

At $|\nu| = 2$, we find self-consistent HF solutions for all of the candidate states in Table II, which coexists with additional spin polarization (either of the SP or SVP type, depending on the sign of J_H). This can explain the experimentally observed [30,31] band resetting for $2 \lesssim |\nu| \lesssim 3$. For instance, the spectrum for the intervalley coherent state is shown in Figs. 6(c) and 6(d) for $\nu = 2$: Increasing the filling fraction ν slightly will lead to Fermi surfaces of completely spin-polarized TBG-like bands, i.e., with half the number of flavors. In magnetic fields, the SP band resetting ($J_H < 0$) will not change its form, while the SVP-related resetting ($J_H > 0$) will continuously develop a finite canting and transform into a SP configuration. We estimate the associated magnetic field scale to be of order of $3T$. Since $J_H < 0$ follows for pure Coulomb interactions [66], we expect the SP to be a more natural candidate; however, $J_H > 0$ is also possible, both theoretically and experimentally, and so we study both signs of J_H in our analysis.

Building on our results for the correlated normal states of MSTG, we analyze the superconducting order parameters in Sec. VII in the different regimes indicated by SC I–III in Fig. 1: When superconductivity coexists with flavor polarization (SC I), the nature of the pairing state depends crucially on the form of the flavor reduction; for the SP ($J_H < 0$) and SVP ($J_H > 0$) polarization that we find around $|\nu| = 2$, we obtain, respectively, a nonunitary triplet and its Hund's partner—a singlet-unitary-triplet admixed phase [27]. For the superconducting phases (SC II) close to but not in the flavor-polarized region, we find triplet pairing to dominate for $J_H < 0$, while the state will either be a singlet or admixed singlet-triplet phases for $J_H > 0$.

The behavior of these superconducting phases in in-plane magnetic fields $B_\parallel$ follows from Ref. [27] where their respective phase diagrams in the temperature-$B_\parallel$ plane have been worked out: In the presence of SP polarization ($J_H < 0$), the critical temperature T_c of the nonunitary triplet is not affected by the Zeemann coupling and suppressed in quadratic order in the in-plane orbital coupling. This naturally explains the strong violation of the Pauli limit [32]. In the other case of SVP polarization ($J_H > 0$), the behavior of T_c of the associated singlet-triplet phase is the same, with the only difference that also the singlet-triplet admixture will gradually transform into a nonunitary triplet with increasing magnetic field. Understanding the reentrant superconducting behavior seen at even larger magnetic fields [32] will require understanding the fate of the correlated parent states, e.g., in Fig. 6, in large magnetic fields, which we leave for future work. Irrespective of whether the order parameter of SC II is a triplet or a singlet-triplet admixed phase, it will continuously transform into a nonunitary triplet [27] upon applying $B_\parallel$, while being eventually suppressed by the orbital coupling. We emphasize that all of the superconducting states we find, including the triplets, are protected [54] against nonmagnetic impurities on the moiré scale, i.e., exhibit an analog of the "Anderson theorem," which is typically expected only for singlet superconductors [72].

For completeness, we also investigate superconductivity close to the charge-neutrality point (SC III), although not prominently seen in current experiments. Here we predict singlet pairing to dominate for the same sign of Hund's coupling $J_H > 0$, and we find triplet pairing near $\nu = 2$.

Because the band structure of MSTG also exhibits Dirac cones, a subset of which persist in most of our dominant particle-hole instabilities [see, e.g., IVC$_-$ in Fig. 3 and Figs. 6(c) and 6(d)related to the preserved $C_{2z}\Theta$ symmetry], we also study the possible WZW terms between superconducting and insulating orders. As discussed in Refs. [25,55] for TBG, these topological terms are associated with and sensitive to the chirality of the Dirac cones in the normal-state band structure. We show here that the set of possibilities in MSTG is greatly reduced as compared to TBG [25], resulting from the reduced flavor degeneracy at $|\nu| \gtrsim 2$ and the impact of the displacement field at $\nu = 0$. As compiled in Table IV, only s-wave singlet pairing is consistent with WZW terms close to $\nu = 0$ (SC I), while both singlet and triplet pairing can have WZW terms in the flavor-polarized region (SC III). The corresponding particle-hole order parameters that form a mutual WZW term with these superconductors feature the sublattice-polarized states that we find to dominate at finite D_0 (in particular, the SSLP$_-$ state) and intervalley-coherent MDW phases.

Unlike all the states studied in the HF analyses of this paper, the MDW phases break translational symmetry at the scale of the moiré period. These MDW states were previously studied [25] in the context of WZW terms in TBG, break the moiré translational symmetry and the valley $\mathrm{U}(1)_v$ symmetry. A closely related "incommensurate Kekulé spiral" appeared in a recent HF numerics study [68] of TBG. (We also note that Kekulé states have been observed in single-layer graphene on a Cu substrate [73] and in the zeroth Landau level [74].) Motivated by these results and our study of WZW terms here, we believe that these types of states are very promising possible additional instabilities in MSTG as well, in models which include the breaking of the $\mathrm{SU}(2)_+ \times \mathrm{SU}(2)_-$ symmetry to the physical $\mathrm{SU}(2)_s$ spin-rotation symmetry; for instance, this could be done in microscopic tight-binding models [43,75–77]. Furthermore, the presence of sufficiently large strain [67,68] might stabilize these MDW states. We leave a detailed energetic study of MDW phases in MSTG for future work.

ACKNOWLEDGMENTS

M. S. S. thanks R. Samajdar for discussions and previous collaborations [27,54] on unconventional superconductivity in moiré systems and acknowledges discussions with T. Lang, A. Läuchli, and R. Fernandes. This research is supported by the National Science Foundation under Grant No. DMR-2002850. This work is also supported by the Simons Collaboration on Ultra-Quantum Matter, which is a grant from the Simons Foundation (Grant No. 651440, S. S.).

Note added.—Recently, two experiments [78,79] appeared online which are consistent with our findings and approach: First, Ref. [78] confirms our conclusion that the graphene-like Dirac cones are stable against interactions. Second, Ref. [79] concludes that spin-polarization (rather than valley polarization) is present around $\nu = 2$, and superconductivity is enhanced by screening the Coulomb repulsion, which is consistent with our pairing mechanism described by Eq. (7.1).

APPENDIX A: MORE ON PERTURBATION THEORY

In this Appendix, we provide more details on the analytical analysis of ordering tendencies in the graphene-like bands and mixing with the TBG-like bands.

1. Order in graphenelike bands

To begin with the analysis of ordering in the graphenelike bands, here we supplement Sec. V A, where only the SP state is discussed. The SLP group of states (SLP$_\pm$ and SSLP$_\pm$) behave differently from the other states, which is why we focus on these state here (the remaining states are analyzed in the Supplemental Material [59] Sec. F 3). To begin with SLP$_\pm$, we have $(Q^g_{\boldsymbol{k}})_{\eta,\eta'} = \delta_{\eta,\eta'}(-\sigma_3 \cos\theta_{\boldsymbol{k}} + \sigma_2 \sin\theta_{\boldsymbol{k}})$, $\boldsymbol{k} \in \mathcal{A}_\eta$, and we need to determine $\theta_{\boldsymbol{k}}$ with $\theta_{\boldsymbol{k}} = \mp\theta_{-\boldsymbol{k}}$ for SLP$_\pm$ due to Θ and C_{2z} by minimizing the energy. The change of the energy as a consequence of this "deformation" is of the form

$$\Delta E_{gg}[\theta_{\boldsymbol{k}}] = \sum_{\eta} \sum_{\boldsymbol{k}\in\mathcal{A}_\eta} [A_{\boldsymbol{k},\eta}(1-\cos\theta_{\boldsymbol{k}}) + B_{\boldsymbol{k},\eta}\sin\theta_{\boldsymbol{k}}] \qquad \text{(A1)}$$

for both SLP$_+$ and SLP$_-$. The explicit expressions for $A_{\boldsymbol{k},\eta}$ and $B_{\boldsymbol{k},\eta}$, which are functions of w_0 and D_0, are given in the Supplemental Material [59] Sec. F 3. From these expressions, it follows that $B_{\boldsymbol{k},\eta} = 0$ and $A_{\boldsymbol{k},\eta} > 0$ for $D_0 = 0$ such that $\Delta E[\theta_{\boldsymbol{k}}]$ is minimized when $\sin\theta_{\boldsymbol{k}} = 0$ (with $\Delta E = 0$), and there is no order in the graphene bands—again in agreement with Sec. III and the HF numerics. Once $D_0 \neq 0$, we get $B_{\boldsymbol{k},\eta} \neq 0$ and $\Delta E < 0$ by choosing a profile with $\sin\theta_{\boldsymbol{k}} \neq 0$. In other words, the graphenelike bands will develop SLP$_\pm$ order for any nonzero D_0, as is visible in the $Q_{\boldsymbol{k}}$ for the SLP$_-$ state close to the K point shown in Fig. 5(b). This ordering in the graphenelike bands gaps out the graphene cone, as can also be seen in our HF band structure in Fig. 3. The energetic gain scales as $g_\pm(\Delta k)^2|D_0|^3$, $g_\pm > 0$, for small D_0 and Δk for the SLP$_\pm$ state; the prefactors differ $g_+ \neq g_-$ due to the symmetry-imposed constraint $\theta_{\boldsymbol{k}} = \mp\theta_{-\boldsymbol{k}}$. For small w_0, we can show that $B_{\boldsymbol{k},\eta} > 0$ such that $g_- > g_+$; i.e., the SLP$_-$ state can gain more energy than the SLP$_+$.

For the SSLP$_-$ state and its Hund's partner SSLP$_+$, which we discuss here explicitly for reasons that become clear shortly, we have $(Q^g_{\boldsymbol{k}})_{\eta,\eta'} = \delta_{\eta,\eta'}(-\sigma_3 \cos\theta_{\boldsymbol{k}} + \sigma_2 \boldsymbol{s} \sin\theta_{\boldsymbol{k}})$, $\boldsymbol{k} \in \mathcal{A}_\eta$. Symmetry imposes $\theta_{\boldsymbol{k}} = \mp\theta_{-\boldsymbol{k}}$ for SSLP$_\pm$. The deformation-related energy change ΔE is found to be again of the form of Eq. (A1); however, here we obtain $B_{\boldsymbol{k},\eta} = 0$ for any D_0 or w_0. This is consistent with $\mathrm{SU}(2)_+ \times \mathrm{SU}(2)_-$ which requires that SSLP$_\pm$ have the same energy. Hence, we show that the graphenelike bands do not develop any direct SSLP$_\pm$ order and gain energy in the process. They will, however, hybridize with the TBG-like bands, as we discuss in Sec. V B, which also gaps out the Dirac cones.

2. Mixing between the graphene and TBG sector

In this part of the Appendix, we outline how the mixing matrices and associated energetic gain, discussed in Sec. V B, can be derived; we refer to the Supplemental Material [59] Sec. F 4 for more details.

Our starting point is product states characterized by a correlator with $Q_{\boldsymbol{k}}$ as given in Eq. (3.13), i.e., without any coherence between the TBG-like and graphenelike bands. In accordance with our analysis of Sec. III, we take $Q^g_{\boldsymbol{k}} = -\sigma_z$ and let $Q^b_{\boldsymbol{k}}$ be any of the candidate orders. To introduce momentum-dependent coherence between these sets of bands, we "deform" $Q_{\boldsymbol{k}}$ by a unitary transformation $U_{\boldsymbol{k}}$ and take

$$Q'_{\boldsymbol{k}} = U_{\boldsymbol{k}} Q_{\boldsymbol{k}} U^\dagger_{\boldsymbol{k}}, \qquad U_{\boldsymbol{k}} = e^{i\Lambda_{\boldsymbol{k}}}, \qquad \Lambda^\dagger_{\boldsymbol{k}} = \Lambda_{\boldsymbol{k}} \in \mathbb{C}^{16\times16} \qquad \text{(A2)}$$

as an ansatz for the correlator. Our goal is to find the optimal momentum-dependent $\Lambda_{\boldsymbol{k}}$ to minimize the energy. Since we are interested in band mixing, we restrict $\Lambda_{\boldsymbol{k}}$ to act as a superposition of ζ_1 and ζ_2, $\Lambda_{\boldsymbol{k}} = \sum_{j=1,2} \mathcal{M}_{\boldsymbol{k},j}\zeta_j$, $\mathcal{M}_{\boldsymbol{k},j} \in \mathbb{C}^{8\times8}$, with ζ_j denoting Pauli matrices acting in the space of TBG-like and graphenelike bands (with index $t = b$, g). Furthermore, $\Lambda_{\boldsymbol{k}}$ will be constrained by the symmetries of the state under consideration.

To illustrate the procedure, let us focus on the IVC$_-$ since this state is found to be dominant in the HF numerics. Choosing $Q^b_{\boldsymbol{k}} = \sigma_y\eta_y$ for concreteness, this state preserves the $C_{2z}\Theta$ symmetry of Table I, which forces $\Lambda_{\boldsymbol{k}}$ to obey $(\Lambda_{\boldsymbol{k}})^* = -\Lambda_{\boldsymbol{k}}$. Furthermore noting that the IVC$_-$ state does not break the $\mathrm{SU}(2)_s$ symmetry (while postponing the consequences of C_{2z} which will relate $\Lambda_{\boldsymbol{k}}$ and $\Lambda_{-\boldsymbol{k}}$), it follows that $\Lambda_{\boldsymbol{k}}$ has to be a momentum-dependent superposition of the 16 generators

$$\zeta_x\sigma_y\eta_{0,x,z}, \qquad \zeta_x\sigma_{0,x,z}\eta_y, \qquad \zeta_y\sigma_{0,x,z}\eta_{0,x,z}, \qquad \zeta_y\sigma_y\eta_y. \qquad \text{(A3)}$$

To simplify further, we can focus on those eight linear combinations [see Eq. (S126) in the Supplemental Material [59] for their explicit form] of the terms in Eq. (A3) that anticommute rather than commute with $Q_{\boldsymbol{k}}$ of the IVC$_-$ state.

The first energetic constraint we take into account is related to the fact that the graphenelike bands of valley $\eta = -$ ($\eta = +$) are far away from the Fermi level at the K (K') point; see Fig. 2. This means that all mixing processes in $\Lambda_{\boldsymbol{k}}$ that induce a finite occupation of the upper or unoccupied states in the lower graphenelike band of valley $\eta = -$ ($\eta = +$) at the K (K') point are suppressed. In the Supplemental Material [59] Sec. F 4, we show that this is equivalent to demanding that $(\mathcal{M}_{\boldsymbol{k}})_{(p',\eta',s'),(p,\mp,s)} = 0$ for $\boldsymbol{k} \in \mathcal{A}_\pm$. This reduces the number of generators further from eight to only four [given in Eq. (S132) of the Supplemental Material [59]]. For each of these four generators Λ_j, $j = 1, 2, 3, 4$, we compute the change of energy associated with the deformation in Eq. (A2) where $U_{\boldsymbol{k}} = e^{i\varphi_{\boldsymbol{k}}\Lambda_j}$. It is found to be of the form

$$\Delta E_{gb}[\varphi_{\boldsymbol{k}}] = \sum_{\boldsymbol{k}\in\mathcal{A}_+} \alpha_{\boldsymbol{k}} \sin^2\varphi_{\boldsymbol{k}} + \beta_{\boldsymbol{k}} \sin\varphi_{\boldsymbol{k}} \cos\varphi_{\boldsymbol{k}}, \qquad \text{(A4)}$$

where $\alpha_{\boldsymbol{k}}$ and $\beta_{\boldsymbol{k}}$ are expressions involving the form factors, the interaction $V(\boldsymbol{q})$, and the band structure (see the

Supplemental Material [59] Sec. F 4 for explicit form) and thus depend on D_0 and w_0. In Eq. (A4), we already take into account the C_{2z} constraint that allows us to write it as a sum over $\boldsymbol{k} \in \mathcal{A}_+$ only.

First, we find $\beta_{\boldsymbol{k}} = 0$ for $D_0 = 0$, and hence, no mixing between the bands as expected by symmetry. However, even when $D_0 \neq 0$, we still obtain $\beta_{\boldsymbol{k}} = 0$ for two of the four generators, while $\beta_{\boldsymbol{k}} \neq 0$ for the other two (say, $\Lambda_{1,2}$) in the chiral limit ($w_0 = 0$). Consequently, at least when w_0 is not too large, the generators $\Lambda_{1,2}$ have to dominate. Which of those remaining two is dominant cannot be determined purely analytically, as it will depend on nonuniversal values of the form factors. The mixing matrix (5.2) for these two candidate generators, Λ_1 and Λ_2 is given by Eqs. (5.3a) and (5.3b), respectively.

Minimizing Eq. (A4) and noting that $\beta_{\boldsymbol{k}}$ scales linearly with D_0 for small D_0 while $\alpha_{\boldsymbol{k}} > 0$ at $D_0 = 0$, we find the scaling of the energetic gain to be $\Delta E_{gb} \sim -g_3(\Delta k)^2 D_0^2$, as stated in the main text.

In the Supplemental Material [59] Sec. F 4, we perform the analogous analysis for all other candidate states. The mixing matrices M^Q in Eq. (5.2) for these states provide some additional consistency checks between analytics and numerics. For instance, the IVC$_+$'s analysis closely parallels the one outlined above for the IVC$_-$: Out of 16 symmetry-allowed generators, only two candidate combinations remain. Interestingly, their associated $\alpha_{\boldsymbol{k}}$ and $\beta_{\boldsymbol{k}}$ in Eq. (A4) are the same (to leading order in D_0) as those of the two IVC$_-$ candidates. Having identified $M^Q_{\boldsymbol{k}}$ in Eq. (5.3) as being dominant by comparison with numerics, we can read off which of the two analytical candidates for the IVC$_+$ must be realized; indeed, we find the same one in numerics [compare Eq. (S139) and Fig. S11 in the Supplemental Material [59]].

[1] A. H. MacDonald, *Bilayer Graphene's Wicked, Twisted Road*, Physics **12**, 12 (2019).

[2] E. Y. Andrei and A. H. MacDonald, *Graphene Bilayers with a Twist*, Nat. Mater. **19**, 1265 (2020).

[3] D. M. Kennes, M. Claassen, L. Xian, A. Georges, A. J. Millis, J. Hone, C. R. Dean, D. N. Basov, A. N. Pasupathy, and A. Rubio, *Moiré Heterostructures as a Condensed-Matter Quantum Simulator*, Nat. Phys. **17**, 155 (2021).

[4] L. Balents, C. R. Dean, D. K. Efetov, and A. F. Young, *Superconductivity and Strong Correlations in Moiré Flat Bands*, Nat. Phys. **16**, 725 (2020).

[5] M. S. Scheurer, *Spectroscopy of Graphene with a Magic Twist*, Nature (London) **572**, 40 (2019).

[6] T. Zaletel, *Stronger-Correlated Superconductivity in Magic-Angle Twisted Trilayer Graphene*, J. Club Condens. Matter Phys. (2021), https://www.condmatjclub.org/?p=4356

[7] Y. Cao, V. Fatemi, A. Demir, S. Fang, S. L. Tomarken, J. Y. Luo, J. D. Sanchez-Yamagishi, K. Watanabe, T. Taniguchi, E. Kaxiras, R. C. Ashoori, and P. Jarillo-Herrero, *Correlated Insulator Behaviour at Half-Filling in Magic-Angle Graphene Superlattices*, Nature (London) **556**, 80 (2018).

[8] Y. Cao, V. Fatemi, S. Fang, K. Watanabe, T. Taniguchi, E. Kaxiras, and P. Jarillo-Herrero, *Unconventional Superconductivity in Magic-Angle Graphene Superlattices*, Nature (London) **556**, 43 (2018).

[9] C. Shen, N. Li, S. Wang, Y. Zhao, J. Tang, J. Liu, J. Tian, Y. Chu, K. Watanabe, T. Taniguchi, R. Yang, Z. Y. Meng, D. Shi, and G. Zhang, *Correlated States in Twisted Double Bilayer Graphene*, Nat. Phys. **16**, 520 (2020).

[10] X. Liu, Z. Hao, E. Khalaf, J. Y. Lee, Y. Ronen, H. Yoo, D. H. Najafabadi, K. Watanabe, T. Taniguchi, A. Vishwanath, and P. Kim, *Tunable Spin-Polarized Correlated States in Twisted Double Bilayer Graphene*, Nature (London) **583**, 221 (2020).

[11] Y. Cao, D. Rodan-Legrain, O. Rubies-Bigorda, J. M. Park, K. Watanabe, T. Taniguchi, and P. Jarillo-Herrero, *Tunable Correlated States and Spin-Polarized Phases in Twisted Bilayer-Bilayer Graphene*, Nature (London) **583**, 215 (2020).

[12] G. W. Burg, J. Zhu, T. Taniguchi, K. Watanabe, A. H. MacDonald, and E. Tutuc, *Correlated Insulating States in Twisted Double Bilayer Graphene*, Phys. Rev. Lett. **123**, 197702 (2019).

[13] G. Chen, L. Jiang, S. Wu, B. Lyu, H. Li, B. L. Chittari, K. Watanabe, T. Taniguchi, Z. Shi, J. Jung, Y. Zhang, and F. Wang, *Evidence of a Gate-Tunable Mott Insulator in a Trilayer Graphene Moiré Superlattice*, Nat. Phys. **15**, 237 (2019).

[14] G. Chen, A. L. Sharpe, P. Gallagher, I. T. Rosen, E. J. Fox, L. Jiang, B. Lyu, H. Li, K. Watanabe, T. Taniguchi, J. Jung, Z. Shi, D. Goldhaber-Gordon, Y. Zhang, and F. Wang, *Signatures of Tunable Superconductivity in a Trilayer Graphene Moiré Superlattice*, Nature (London) **572**, 215 (2019).

[15] G. Chen, A. L. Sharpe, E. J. Fox, Y.-H. Zhang, S. Wang, L. Jiang, B. Lyu, H. Li, K. Watanabe, T. Taniguchi, Z. Shi, T. Senthil, D. Goldhaber-Gordon, Y. Zhang, and F. Wang, *Tunable Correlated Chern Insulator and Ferromagnetism in a Moiré Superlattice*, Nature (London) **579**, 56 (2020).

[16] J. M. B. Lopes Dos Santos, N. M. R. Peres, and A. H. Castro Neto, *Graphene Bilayer with a Twist: Electronic Structure*, Phys. Rev. Lett. **99**, 256802 (2007).

[17] R. Bistritzer and A. H. MacDonald, *Moiré Bands in Twisted Double-Layer Graphene*, Proc. Natl. Acad. Sci. U.S.A. **108**, 12233 (2011).

[18] J. M. B. Lopes Dos Santos, N. M. R. Peres, and A. H. Castro Neto, *Continuum Model of the Twisted Graphene Bilayer*, Phys. Rev. B **86**, 155449 (2012).

[19] A. Kerelsky, L. J. McGilly, D. M. Kennes, L. Xian, M. Yankowitz, S. Chen, K. Watanabe, T. Taniguchi, J. Hone, C. Dean, A. Rubio, and A. N. Pasupathy, *Maximized Electron Interactions at the Magic Angle in Twisted Bilayer Graphene*, Nature (London) **572**, 95 (2019).

[20] Y. Cao, D. Rodan-Legrain, J. M. Park, F. N. Yuan, K. Watanabe, T. Taniguchi, R. M. Fernandes, L. Fu, and P. Jarillo-Herrero, *Nematicity and Competing Orders in Superconducting Magic-Angle Graphene*, Science **372**, 264 (2021).

[21] C. Rubio-Verdú, S. Turkel, L. Song, L. Klebl, R. Samajdar, M. S. Scheurer, J. W. F. Venderbos, K. Watanabe, T. Taniguchi, H. Ochoa, L. Xian, D. Kennes, R. M. Fernandes, Á. Rubio, and A. N. Pasupathy, *Universal Moiré Nematic Phase in Twisted Graphitic Systems*, Nat. Phys. **18**, 196 (2022).

[22] R. Samajdar, M. Scheurer, S. Turkel, C. Rubio-Verdú, A. Pasupathy, J. Venderbos, and R. M. Fernandes, *Electric-Field-Tunable Electronic Nematic Order in Twisted Double-Bilayer Graphene*, 2D Mater. **8**, 034005 (2021).

[23] U. Zondiner, A. Rozen, D. Rodan-Legrain, Y. Cao, R. Queiroz, T. Taniguchi, K. Watanabe, Y. Oreg, F. von Oppen, A. Stern, E. Berg, P. Jarillo-Herrero, and S. Ilani, *Cascade of Phase Transitions and Dirac Revivals in Magic-Angle Graphene*, Nature (London) **582**, 203 (2020).

[24] D. Wong, K. P. Nuckolls, M. Oh, B. Lian, Y. Xie, S. Jeon, K. Watanabe, T. Taniguchi, B. A. Bernevig, and A. Yazdani, *Cascade of Electronic Transitions in Magic-Angle Twisted Bilayer Graphene*, Nature (London) **582**, 198 (2020).

[25] M. Christos, S. Sachdev, and M. S. Scheurer, *Superconductivity, Correlated Insulators, and Wess-Zumino-Witten Terms in Twisted Bilayer Graphene*, Proc. Natl. Acad. Sci. U.S.A. **117**, 29543 (2020).

[26] J. Kang, B. A. Bernevig, and O. Vafek, *Cascades between Light and Heavy Fermions in the Normal State of Magic Angle Twisted Bilayer Graphene*, Phys. Rev. Lett. **127**, 266402 (2021).

[27] M. S. Scheurer and R. Samajdar, *Pairing in Graphene-Based Moiré Superlattices*, Phys. Rev. Research **2**, 033062 (2020).

[28] C. Zhang, T. Zhu, S. Kahn, S. Li, B. Yang, C. Herbig, X. Wu, H. Li, K. Watanabe, T. Taniguchi, S. Cabrini, A. Zettl, M. P. Zaletel, F. Wang, and M. F. Crommie, *Visualizing Delocalized Correlated Electronic States in Twisted Double Bilayer Graphene*, Nat. Commun. **12**, 2516 (2021).

[29] X. Liu, C.-L. Chiu, J. Y. Lee, G. Farahi, K. Watanabe, T. Taniguchi, A. Vishwanath, and A. Yazdani, *Spectroscopy of a Tunable Moiré System with a Correlated and Topological Flat Band*, Nat. Commun. **12**, 2732 (2021).

[30] J. M. Park, Y. Cao, K. Watanabe, T. Taniguchi, and P. Jarillo-Herrero, *Tunable Strongly Coupled Superconductivity in Magic-Angle Twisted Trilayer Graphene*, Nature (London) **590**, 249 (2021).

[31] Z. Hao, A. M. Zimmerman, P. Ledwith, E. Khalaf, D. H. Najafabadi, K. Watanabe, T. Taniguchi, A. Vishwanath, and P. Kim, *Electric Field-Tunable Superconductivity in Alternating-Twist Magic-Angle Trilayer Graphene*, Science **371**, 1133 (2021).

[32] Y. Cao, J. M. Park, K. Watanabe, T. Taniguchi, and P. Jarillo-Herrero, *Large Pauli Limit Violation and Reentrant Superconductivity in Magic-Angle Twisted Trilayer Graphene*, arXiv:2103.12083.

[33] E. Khalaf, A. J. Kruchkov, G. Tarnopolsky, and A. Vishwanath, *Magic Angle Hierarchy in Twisted Graphene Multilayers*, Phys. Rev. B **100**, 085109 (2019).

[34] S. Carr, C. Li, Z. Zhu, E. Kaxiras, S. Sachdev, and A. Kruchkov, *Ultraheavy and Ultrarelativistic Dirac Quasiparticles in Sandwiched Graphenes*, Nano Lett. **20**, 3030 (2020).

[35] C. Mora, N. Regnault, and B. A. Bernevig, *Flatbands and Perfect Metal in Trilayer Moiré Graphene*, Phys. Rev. Lett. **123**, 026402 (2019).

[36] D. Călugăru, F. Xie, Z.-D. Song, B. Lian, N. Regnault, and B. A. Bernevig, *Twisted Symmetric Trilayer Graphene: Single-Particle and Many-Body Hamiltonians and Hidden Nonlocal Symmetries of Trilayer Moiré Systems with and without Displacement Field*, Phys. Rev. B **103**, 195411 (2021).

[37] J. Shin, B. L. Chittari, and J. Jung, *Stacking and Gate Tunable Topological Flat Bands, Gaps and Anisotropic Strip Patterns in Twisted Trilayer Graphene*, Phys. Rev. B **104**, 045413 (2021).

[38] C. Lei, L. Linhart, W. Qin, F. Libisch, and A. H. MacDonald, *Mirror Symmetry Breaking and Lateral Stacking Shifts in Twisted Trilayer Graphene*, Phys. Rev. B **104**, 035139 (2021).

[39] A. Ramires and J. L. Lado, *Emulating Heavy Fermions in Twisted Trilayer Graphene*, Phys. Rev. Lett. **127**, 026401 (2021).

[40] Y. W. Choi and H. J. Choi, *Dichotomy of Electron-Phonon Coupling in Graphene Moire Flat Bands*, Phys. Rev. Lett. **127**, 167001 (2021).

[41] E. Lake and T. Senthil, *Re-entrant Superconductivity through a Quantum Lifshitz Transition in Twisted Trilayer Graphene*, Phys. Rev. B **104**, 174505 (2021).

[42] W. Qin and A. H. MacDonald, *In-Plane Critical Magnetic Fields in Magic-Angle Twisted Trilayer Graphene*, Phys. Rev. Lett. **127**, 097001 (2021).

[43] A. Fischer, Z. A. H. Goodwin, A. A. Mostofi, J. Lischner, D. M. Kennes, and L. Klebl, *Unconventional Superconductivity in Magic-Angle Twisted Trilayer Graphene*, npj Quantum Mater. **7**, 5 (2022).

[44] Y.-Z. Chou, F. Wu, J. D. Sau, and S. D. Sarma, *Correlation-Induced Triplet Pairing Superconductivity in Graphene-Based Moiré Systems*, Phys. Rev. Lett. **127**, 217001 (2021).

[45] M. Xie and A. MacDonald, *Nature of the Correlated Insulator States in Twisted Bilayer Graphene*, Phys. Rev. Lett. **124**, 097601 (2020).

[46] N. Bultinck, E. Khalaf, S. Liu, S. Chatterjee, A. Vishwanath, and M. P. Zaletel, *Ground State and Hidden Symmetry of Magic Angle Graphene at Even Integer Filling*, Phys. Rev. X **10**, 031034 (2020).

[47] S. Liu, E. Khalaf, J. Y. Lee, and A. Vishwanath, *Nematic Topological Semimetal and Insulator in Magic-Angle Bilayer Graphene at Charge Neutrality*, Phys. Rev. Research **3**, 013033 (2021).

[48] Y.-D. Liao, X.-Y. Xu, Z.-Y. Meng, and J. Kang, *Correlated Insulating Phases in the Twisted Bilayer Graphene**, Chin. Phys. B **30**, 017305 (2021).

[49] N. Bultinck, S. Chatterjee, and M. P. Zaletel, *Mechanism for Anomalous Hall Ferromagnetism in Twisted Bilayer Graphene*, Phys. Rev. Lett. **124**, 166601 (2020).

[50] Y. Zhang, K. Jiang, Z. Wang, and F. Zhang, *Correlated Insulating Phases of Twisted Bilayer Graphene at Commensurate Filling Fractions: A Hartree-Fock Study*, Phys. Rev. B **102**, 035136) (2020).

[51] P. Stepanov, I. Das, X. Lu, A. Fahimniya, K. Watanabe, T. Taniguchi, F. H. L. Koppens, J. Lischner, L. Levitov, and

D. K. Efetov, *Untying the Insulating and Superconducting Orders in Magic-Angle Graphene*, Nature (London) **583**, 375 (2020).

[52] X. Liu, Z. Wang, K. Watanabe, T. Taniguchi, O. Vafek, and J. I. A. Li, *Tuning Electron Correlation in Magic-Angle Twisted Bilayer Graphene Using Coulomb Screening*, Science **371**, 1261 (2021).

[53] Y. Saito, J. Ge, K. Watanabe, T. Taniguchi, and A. F. Young, *Independent Superconductors and Correlated Insulators in Twisted Bilayer Graphene*, Nat. Phys. **16**, 926 (2020).

[54] R. Samajdar and M. S. Scheurer, *Microscopic Pairing Mechanism, Order Parameter, and Disorder Sensitivity in Moiré Superlattices: Applications to Twisted Double-Bilayer Graphene*, Phys. Rev. B **102**, 064501 (2020).

[55] E. Khalaf, S. Chatterjee, N. Bultinck, M. P. Zaletel, and A. Vishwanath, *Charged Skyrmions and Topological Origin of Superconductivity in Magic-Angle Graphene*, Sci. Adv. **7**, eabf5299 (2021).

[56] N. N. T. Nam and M. Koshino, *Lattice Relaxation and Energy Band Modulation in Twisted Bilayer Graphene*, Phys. Rev. B **96**, 075311 (2017).

[57] S. Carr, S. Fang, Z. Zhu, and E. Kaxiras, *Exact Continuum Model for Low-Energy Electronic States of Twisted Bilayer Graphene*, Phys. Rev. Research **1**, 013001 (2019).

[58] S. Turkel, J. Swann, Z. Zhu, M. Christos, K. Watanabe, T. Taniguchi, S. Sachdev, M. S. Scheurer, E. Kaxiras, C. R. Dean, and A. N. Pasupathy, *Twistons in a Sea of Magic*, arXiv:2109.12631.

[59] See Supplemental Material at http://link.aps.org/supplemental/10.1103/PhysRevX.12.021018 for details on the continuum model used in our analytics and numerics, additional derivations and details of our analytic results, and additional numerical data not presented in the main text.

[60] G. Tarnopolsky, A. J. Kruchkov, and A. Vishwanath, *Origin of Magic Angles in Twisted Bilayer Graphene*, Phys. Rev. Lett. **122**, 106405 (2019).

[61] B. A. Bernevig, Z.-D. Song, N. Regnault, and B. Lian, *Twisted Bilayer Graphene. III. Interacting Hamiltonian and Exact Symmetries of Twisted Bilayer Graphene*, Phys. Rev. B **103**, 205413 (2021).

[62] B. Lian, Z.-D. Song, N. Regnault, D. K. Efetov, A. Yazdani, and B. A. Bernevig, *Twisted Bilayer Graphene. IV. Exact Insulator Ground States and Phase Diagram of Twisted Bilayer Graphene*, Phys. Rev. B **103**, 205414 (2021).

[63] J. Kang and O. Vafek, *Strong Coupling Phases of Partially Filled Twisted Bilayer Graphene Narrow Bands*, Phys. Rev. Lett. **122**, 246401 (2019).

[64] A. H. Castro Neto, F. Guinea, N. M. R. Peres, K. S. Novoselov, and A. K. Geim, *The Electronic Properties of Graphene*, Rev. Mod. Phys. **81**, 109 (2009).

[65] Note that the term c_2, which comes from the Hartree term, turns out to be numerically very small.

[66] S. Chatterjee, N. Bultinck, and M. P. Zaletel, *Symmetry Breaking and Skyrmionic Transport in Twisted Bilayer Graphene*, Phys. Rev. B **101**, 165141 (2020).

[67] D. E. Parker, T. Soejima, J. Hauschild, M. P. Zaletel, and N. Bultinck, *Strain-Induced Quantum Phase Transitions in Magic-Angle Graphene*, Phys. Rev. Lett. **127**, 027601 (2021).

[68] Y. H. Kwan, G. Wagner, T. Soejima, M. P. Zaletel, S. H. Simon, S. A, Parameswaran, and N. Bultinck, *Kekulé Spiral Order at All Nonzero Integer Fillings in Twisted Bilayer Graphene*, Phys. Rev. X **11**, 041063 (2021).

[69] P. M. R. Brydon, S. Das Sarma, H.-Y. Hui, and J. D. Sau, *Odd-Parity Superconductivity from Phonon-Mediated Pairing: Application to* $\mathrm{Cu}_x\mathrm{Bi}_2\mathrm{Se}_3$, Phys. Rev. B **90**, 184512 (2014).

[70] M. S. Scheurer, *Mechanism, Time-Reversal Symmetry, and Topology of Superconductivity in Noncentrosymmetric Systems*, Phys. Rev. B **93**, 174509 (2016).

[71] S. Chatterjee, M. Ippoliti, and M. P. Zaletel, *Skyrmion Superconductivity: DMRG Evidence for a Topological Route to Superconductivity*, arXiv:2010.01144.

[72] A. P. Mackenzie and Y. Maeno, *The superconductivity of* $\mathrm{Sr}_2\mathrm{RuO}_4$ *and the Physics of Spin-Triplet Pairing*, Rev. Mod. Phys. **75**, 657 (2003).

[73] C. Gutiérrez, C.-J. Kim, L. Brown, T. Schiros, D. Nordlund, E. B. Lochocki, K. M. Shen, J. Park, and A. N. Pasupathy, *Imaging Chiral Symmetry Breaking from Kekulé Bond Order in Graphene*, Nat. Phys. **12**, 950 (2016).

[74] S.-Y. Li, Y. Zhang, L.-J. Yin, and L. He, *Scanning Tunneling Microscope Study of Quantum Hall Isospin Ferromagnetic States in the Zero Landau Level in a Graphene Monolayer*, Phys. Rev. B **100**, 085437 (2019).

[75] A. O. Sboychakov, A. V. Rozhkov, A. L. Rakhmanov, and F. Nori, *Many-Body Effects in Twisted Bilayer Graphene at Low Twist Angles*, Phys. Rev. B **100**, 045111 (2019).

[76] A. O. Sboychakov, A. V. Rozhkov, A. L. Rakhmanov, and F. Nori, *Spin Density Wave and Electron Nematicity in Magic-Angle Twisted Bilayer Graphene*, Phys. Rev. B **102**, 155142 (2020).

[77] A. Fischer, L. Klebl, C. Honerkamp, and D. M. Kennes, *Spin-Fluctuation-Induced Pairing in Twisted Bilayer Graphene*, Phys. Rev. B **103**, L041103 (2021).

[78] H. Kim, Y. Choi, C. Lewandowski, A. Thomson, Y. Zhang, R. Polski, K. Watanabe, T. Taniguchi, J. Alicea, and S. Nadj-Perge, *Spectroscopic Signatures of Strong Correlations and Unconventional Superconductivity in Twisted Trilayer Graphene*, arXiv:2109.12127.

[79] X. Liu, N. J. Zhang, K. Watanabe, T. Taniguchi, and J. I. A. Li, *Coulomb Screening and Thermodynamic Measurements in Magic-Angle Twisted Trilayer Graphene*, arXiv:2108.03338.